RABI OSCILLATIONS IN STRONGLY- DRIVEN

MAGNETIC RESONANCE SYSTEMS

by

Edward F. Thenell III

A dissertation submitted to the faculty of
The University of Utah
in partial fulfillment of the requirements for the degree of

Doctor of Philosophy

in

Physics

Department of Physics and Astronomy

The University of Utah

May 2017

The University of Utah Graduate School

STATEMENT OF DISSERTATION APPROVAL

The dissertation of **Edward F. Thenell III**

has been approved by the following supervisory committee members:

Brian Saam	, Chair	**12/9/2016** Date Approved
Christoph Boehme	, Member	**12/9/2016** Date Approved
Mikhail E. Raikh	, Member	**12/19/2016** Date Approved
Stephane Louis LeBohec	, Member	Date Approved
Eun-Kee Jeong	, Member	**12/9/2016** Date Approved

and by **Benjamin C. Bromley** , Chair of

the Department of **Physics and Astronomy**

and by David B. Kieda, Dean of The Graduate School.

ABSTRACT

This dissertation is focused on an exploration of the strong-drive regime in magnetic resonance, in which the amplitude of the linearly-oscillating driving field is on order the quantizing field. This regime is rarely accessed in traditional magnetic resonance experiments, due primarily to signal-to-noise concerns in thermally-polarized samples which require the quantizing field to take on values much larger than those practically attainable in the tuned LC circuits which typically produce the driving field. However, such limitations are circumvented in the two primary experiments discussed herein, allowing for novel and systematic exploration of this magnetic resonance regime.

First, spectroscopic data was taken on 129Xe nuclear spins, hyperpolarized via spin-exchange optical pumping (SEOP). Since SEOP creates a nuclear spin polarization that is independent of the quantizing field magnitude, magnetic resonance experiments can be performed at arbitrarily low resonance frequency, where the strong drive regime can be trivially accessed. The spectroscopic data are attained by studying the amplitude and frequency of 129Xe Rabi oscillations as a function of the driving frequency, for various values of the applied field and driving field magnitudes. These Rabi oscillations can be observed in real-time via an indirect optical detection scheme, designed and built in the Saam lab.

Second, we explore the spectrum of Rabi oscillations of protons in a conventional water sample, acquired under longitudinal field modulation, which reproduces the conditions of the strong drive regime in the rotating frame. The modulation regimes on which this work focuses tend to create multiple strong frequency components, as well as exhibiting a strong sensitivity to the phase of the modulation field. To account for these complications, we use a phase-averaged Fourier transform analysis, with which modulation-related effects on the Rabi dynamics can be studied systematically by tracking the position and magnitude of components in the Rabi oscillation Fourier spectrum.

Additional material covers a study of longitudinal nuclear spin relaxation times in two organic semiconducting polymers, MEH-PPV and DOO-PPV, with the intention of informing the feasibility of angular momentum transfer to the nuclear spins from spin-polarized charge carriers in active spintronic devices.

TABLE OF CONTENTS

LIST OF FIGURES

CHAPTER 1

INTRODUCTION

The primary thread that connects the topics addressed in this work is experimental nuclear magnetic resonance (NMR). In particular, an exploration of the strong-drive regime – a rarely-accessible regime defined by an excitation field whose amplitude is on order the Zeeman energy splitting – has been of paramount importance for the two most substantial projects addressed here.

The strong-drive regime can be accessed in any driven two-level system. Such systems are ubiquitous in modern physics, arising in such varied fields as atomic physics, quantum dots, and of particular importance to this work, magnetic resonance. For various reasons which will be covered in detail at several points throughout this work, though mostly a consequence of the weak nuclear magnetic moment, the strong-drive regime is practically unattainable in conventional NMR experiments. However, there are a number of two-level systems, many of which are the subject of a great deal of current research, in which the strong-drive regime is either easily accessible (unconventional MR schemes) or entirely unavoidable (ultrafast atomic spectroscopy). These research areas are of continued interest to the physics community and drive

interest in further understanding of the strong-drive regime. Here, we look to use the dual-expertise of the Saam lab – NMR and spin-exchange optical pumping – to investigate the fundamental physics of the strong drive regime through novel use of conventional NMR systems.

In this work, we begin to characterize the strong-drive regime in two distinct magnetic-resonance systems: (1) hyperpolarized ^{129}Xe gas, in which the large field-independent nuclear polarization allows access to the strong-drive regime by significantly reducing the energy of the unperturbed Hamiltonian (without sacrificing measurement sensitivity); and (2) conventional high-field liquid ^{1}H (proton) NMR, augmented with a small, slowly varying longitudinal field, which allows access to the strong-drive regime within the so-called *rotating frame*. We compare both of these systems with appropriate models of the respective Rabi-oscillation spin dynamics, and then proceed to discuss the extent to which we observe spectroscopic evidence for *dressed states* – states that consist of nontrivial admixtures of the conventional two-level eigenstates with the driving field, which is now large enough that its presence cannot be treated perturbatively.

To orient readers along these lines, I will begin here with a general introduction to magnetic resonance, focusing on conventional approaches to the theory that inform the vast majority of the experimental work done in the field. As Chapter 2 involves experimental work with noble gases that have been hyperpolarized via spin-exchange optical pumping (SEOP), I will transition into a discussion on this topic, with emphasis on how SEOP addresses some of the fundamental limitations of conventional NMR and

how hyperpolarized gases are particularly well-suited to exploration of the strong-drive regime. I will also briefly discuss the theory which describes strongly-driven two-level systems and how similar theory can be applied to weakly driven two-level systems with an added modulation of the energy splitting. General prerequisite knowledge can be found in refs. [1-4].

1.1 Conventional NMR: Inside the Rotating Wave Approximation

The purpose of this section is to familiarize the reader with the basics of magnetic resonance theory, including semiclassical and quantum mechanical approaches, and a brief overview of the history of the technique and its impact on science as a whole. Much of the discussion in this section is derived from - and covered in more detail within – the three canonical NMR textbooks [5-7].

1.1.1 A Brief History of NMR

When telling the story of magnetic resonance, one must necessarily begin with the pioneering research of Isidor Isaac Rabi on molecular beams, which constitutes the first experimental observation of magnetic resonance. While the famous Stern-Gerlach experiment [8] had confirmed the magnetic moment of the electron in the early 1920s, and modifications on that model had showed by the early 1930s that certain nuclei possessed intrinsic magnetic moments as well, Rabi was the first to directly measure the magnetic moment of a nucleus, the first being Lithium, by subjecting a beam of molecules passing through a homogeneous, static magnetic field to radio frequency (rf)

radiation [9]. Rabi found that, at a specific frequency, this rf radiation would cause a small deflection of the beam, indicating resonant absorption. For this groundbreaking observation, originally published in 1939, Rabi was awarded the Nobel Prize for Physics in 1944.

The next major step in the development of NMR did not take long, as Felix Bloch and Edward Purcell independently developed, and subsequently published within mere weeks of each other, methods with which Rabi's observations could be expanded to liquids and solids [10,11]. For this, and their independent contributions to early theories of NMR relaxation processes, Bloch and Purcell shared the Nobel Prize for Physics in 1952.

It should not come as a surprise that these developments came in rapid succession at the time that they did. World War II ushered in massive advances in rf electronics in service of then-state-of-the-art radar systems, and many of the scientists that helped make these advances moved on to academic pursuits after the war's conclusion. Among them was none other than Edward Purcell who, as we have already seen, can be counted among the most important early contributors to the field of NMR.

The next several decades brought myriad advances which have helped NMR develop into the ubiquitous scientific tool that it is today. Although there are far too many to list in detail, some particularly crucial advances which have immediate bearing on this work have come from Russell Varian, who was first to develop a commercial NMR system [12,13], Alfred G. Redfield, whose influential first work in the field presented a comprehensive theory of relaxation and corrected mistakes in the theories

put forth by Bloch and Purcell [14], Erwin Hahn, whose discovery of spin-echoes can be considered the first experiment in pulsed-NMR [15-17], Albert Overhauser, whose discovery of the Overhauser effect effectively invented the field of dynamic nuclear polarization (DNP) [18], and finally, Richard Ernst, who pioneered the use of Fourier transform theory in the field of NMR [19].

1.1.2 Pulsed-NMR: A Semiclassical Treatment

We begin by considering a magnetic moment, $\vec{\mu}$, and its interaction with an external magnetic field, $\vec{B}$. The torque exerted on $\vec{\mu}$ by $\vec{B}$ is given as

$$\vec{\tau} = \vec{\mu} \times \vec{B} \tag{1.1}$$

but since the net torque is defined as the rate of change of a system's angular momentum, and the moment can be rewritten as $\gamma \vec{I}$, where $\vec{I}$ and γ are the spin and gyromagnetic ratio of the particle in consideration, respectively, Eq. (1.1) can be re-written as

$$\frac{d\vec{\mu}}{dt} = \vec{\mu} \times \left(\gamma \vec{B} \right) . \tag{1.2}$$

Assuming a static external magnetic field, the solution to this differential equation shows that the moment will *precess* about the static field. It should be noted that this process conserves energy, as the magnetic energy of the system is given as $E = -\vec{\mu} \bullet \vec{B}$ and the precession behavior predicted by Eq. (1.2) will not change the angle between the moment and the field.

Now, consider the same system, with the addition of a magnetic field, $\overrightarrow{B_1}(t)$, rotating at frequency ω and oriented in the plane perpendicular to the static field, now called $\overrightarrow{B_0}$, for clarity. This addition can be handled by transforming into a reference frame that rotates at the same frequency as $\overrightarrow{B_1}$, henceforth referred to as the *rotating frame*. It can be shown that, in this frame, the effective magnetic field takes the form, [6]

$$\vec{B}_{eff} = B_1\hat{x} + \left(B_0 - \frac{\omega}{\gamma}\right)\hat{z}. \tag{1.3}$$

Note that, for $\omega = \omega_0 = \gamma B_0$, the static field that is present in the lab frame is transformed away in the rotating frame. This serves as our definition of the resonance condition, and this resonant frequency is called the Larmor frequency.

The most important take-away from Eq. (1.3) is that, in the rotating frame, $\vec{B}_{eff}$ is static and, in general, not parallel to the quantization axis established by $\overrightarrow{B_0}$ in the lab frame. This means that any moments that were aligned with the static field in the lab frame will *nutate* about the effective field in the rotating frame. In contrast to precession, this process changes the magnetic energy of the system, as the angle between $\overrightarrow{B_0}$ and $\vec{\mu}$ will accumulate for as long as the rotating field remains on.

The frequency of this oscillation is given as $\Omega = \gamma\left|\overrightarrow{B_{eff}}\right|$ which takes on a minimum value of γB_1 when $\omega = \omega_0$. These oscillations are named for I. I. Rabi, who gave a general quantum mechanical description of the behavior that we have derived

semiclassically here.

This simple picture provides all basic information necessary to conceptualize a pulsed-NMR experiment, as illustrated in Figure 1.1. In such an experiment, B_1 is turned on for a controlled duration τ such that the sample magnetization nutates through an angle $\theta = \Omega\tau$, in the rotating frame for resonant excitation. Once B_1 is turned off, the moment will precess about B_0 at the Larmor frequency. This precession can be detected inductively by a nearby pickup coil, often the very same coil used to transmit the excitation pulse.

1.1.3 Quantum Mechanical Treatment: The Liouville Equation

Though a semiclassical treatment can effectively illustrate many of the fundamental aspects of the magnetic resonance effect, establishing a quantum formalism will be key for addressing advanced topics in magnetic resonance later in this work. The Hamiltonian of a single, noninteracting spin in a magnetic field is simply the Zeeman Hamiltonian, written as

$$H_Z = -\vec{\mu} \bullet \vec{B} = -\gamma \hbar B_0 I_z \tag{1.4}$$

This gives energy eigenvalues

$$E_m = -\gamma \hbar B_0 m_I \tag{1.5}$$

where m_I is the magnetic spin quantum number with respect to the quantizing field.

The simplest way to show the compatibility between our semiclassical treatment and

a rigorous quantum mechanical treatment is to consider the Quantum Liouville equation, which shows that the time derivative of an operator can be calculated by the following commutator relation with the Hamiltonian of the system,

$$\frac{d}{dt}\left\langle \hat{O} \right\rangle = \frac{i}{\hbar}\left\langle \psi \left| \left[\hat{H}, \hat{O} \right] \right| \psi \right\rangle . \tag{1.6}$$

This can be applied to calculate the time evolution of a magnetic moment, with $\hat{\mu} = \gamma \hbar \hat{I}$. Noting that the spin operators can be recast as linear combinations of angular momentum raising and lowering operators, and recalling that $\left[\hat{A}, \hat{B} \right] = \hat{A}\hat{B} - \hat{B}\hat{A}$, one can show that

$$\frac{d}{dt}\left\langle \hat{\mu} \right\rangle = \frac{i}{\hbar}\left\langle \psi \left| \left[\hat{H}_Z, \hat{\mu} \right] \right| \psi \right\rangle = \left\langle \hat{\mu} \right\rangle \times \gamma \vec{B} . \tag{1.7}$$

This, remarkably, is the same equation of motion from our classical treatment, Eq. (1.2). That we can arrive at the same equation of motion through these two different formalisms shows one important reason why magnetic resonance has been such a fruitful area of research over the last half-century, as a system whose fundamental phenomena adhere to classical intuition, yet provide insight into purely quantum mechanical processes [5,6,10,11,18,20].

1.1.4 Quantum Mechanical Treatment: The Rabi Problem

In consideration of the work presented in this dissertation, a different approach to the magnetic resonance problem may prove more insightful. Although I. I. Rabi has already been mentioned in this thesis for his groundbreaking observation of magnetic

resonance in molecular beams, perhaps his most influential contribution to the field came with his approach to solving a now ubiquitous quantum mechanical problem, the driven two-level system. This is a problem of enormous practical importance and, most interestingly, one of very few in time-dependent perturbation theory that, under the proper conditions, can be solved exactly.

Again, one begins with a Hamiltonian, albeit a more generalized one in this case,

$$\hat{H}_0 = \begin{pmatrix} E_\uparrow & 0 \\ 0 & E_\downarrow \end{pmatrix}, \tag{1.8}$$

then we consider a small perturbing potential, which corresponds to a perpendicular rotating field,

$$V(t) = \gamma \begin{pmatrix} 0 & e^{i\omega t} \\ e^{-i\omega t} & 0 \end{pmatrix}. \tag{1.9}$$

This gives a total Hamiltonian of $\hat{H}_{tot} = \hat{H}_0 + \hat{V}(t)$, for which we will calculate the evolution of $\psi = c_1(t)\left|\uparrow\right\rangle + c_2(t)\left|\downarrow\right\rangle$. Calculating the state coefficients will give the evolution of the system under drive.

For the initial conditions $c_1(0) = 1$ and $c_2(0) = 0$, one can derive the famous Rabi equation,

$$\left|c_1(t)\right|^2 = \frac{\gamma^2}{\gamma^2 + \frac{\hbar^2}{4}\Delta^2} \sin^2\left(\sqrt{\frac{\gamma^2}{\hbar^2} + \frac{\Delta^2}{4}}\, t\right), \tag{1.10}$$

where $\Delta = \omega - \omega_0$ and $\omega_0 = \left(E_\downarrow - E_\uparrow\right)/\hbar$. This shows that the probability to find the spin

in the "up" state oscillates in time at a frequency that depends both on the strength of the perturbing potential and the proximity of the driving frequency to resonance. The dependences of both the oscillation amplitude and frequency on the frequency of the applied field are shown in Figure 1.2. These, of course, are the well-known Rabi oscillations, which can be observed in a variety of two-level systems [21-23] including single-spin resonances [24].

Note that detuning the driving frequency from resonance increases the Rabi frequency while decreasing the amplitude of the oscillatory behavior, corresponding to a decreased probability for the driving field to induce transitions between the two levels.

It should also be noted that all of our theoretical treatments of this system, thus far, have assumed the presence of a *rotating* field to drive transitions between the spin states. While this is a convenient assumption for theoretical treatments, as it allows for exact solutions in all three of the example cases considered thus far, creating rotating fields in the lab can prove practically quite difficult. Instead, the vast majority of NMR experiments are performed with *linearly-oscillating* driving fields of the form,

$$\overrightarrow{B_1}(t) = 2B_1 \cos(\omega t)\hat{x} \,. \tag{1.11}$$

A linearly-oscillating field of this form can be decomposed into two counter-rotating components, as such,

$$\overrightarrow{B_1}(t) = B_1(\cos(\omega t)\hat{x} + \sin(\omega t)\hat{y}) + B_1(\cos(\omega t)\hat{x} - \sin(\omega t)\hat{y}) \tag{1.12}$$

where the first term represents a field rotating at frequency ω and the second represents a counter-rotating field with frequency $-\omega$. In the limit that $B_0 >> B_1$ for

near-resonant excitation, the negative frequency component can be readily ignored as it gives $\Delta \approx 2\omega_0$ which forces its effect on transition probabilities to be vanishingly small, per Eq. (1.10). Disregarding the negative frequency component of the linearly-oscillating field is known as the rotating wave approximation (RWA), and it is made in the overwhelming majority of magnetic resonance experiments across all relevant fields of research, not so much out of mathematical convenience as technical necessity, as we will see in the next section.

1.1.5 Polarization: The Limits of NMR Sensitivity and How to Get Around Them

While magnetic resonance has repeatedly proved its utility over its lifetime as a scientific tool, it has also shown itself to be a relatively insensitive one – NMR in particular. Understanding the nature of this inherent insensitivity is key to understanding spin-exchange optical pumping, a particularly ingenious method for circumventing this limitation.

By placing a spin in an external magnetic field, a quantization axis for the spin degree of freedom is established and the energy degeneracy of the two eigenstates for a spin-1/2 particle is lifted. Lifting this degeneracy establishes a thermal equilibrium polarization, given that the spin ensemble interacts with a thermal bath, as there is now a thermodynamically-preferred "low energy state" that the particles can occupy. This polarization for an ensemble of spin-1/2 nuclei can be calculated via Boltzmann statistics as

$$P = \frac{e^{\frac{\hbar\gamma B}{2kT}} - e^{-\frac{\hbar\gamma B}{2kT}}}{e^{\frac{\hbar\gamma B}{2kT}} + e^{-\frac{\hbar\gamma B}{2kT}}} = \tanh\left(\frac{\hbar\gamma B}{2kT}\right). \tag{1.13}$$

For protons in a 2 T field at room temperature, this calculation yields a polarization on order 1E-6. This low polarization is primarily a consequence of the weak moment of nuclear spins – nearly three orders of magnitude smaller than the electron moment. Another consequence of the weak moment is that the field that results from the precession of these nuclei is small. As a result, a conventional liquid NMR experiment (with linewidths on order 1 Hz) requires a sample with at least $\approx 10^{19}$ nuclear spins to achieve a signal-to-noise ratio (SNR) ≥ 1, which excludes the possibility of performing experiments on nonmacroscopic samples such as thin films, and severely limits one's ability to perform experiments at low field, as the loss in signal that results from decreasing the field by, say, a factor of 10 cannot be made up by increasing the size of the sample by the same factor, as additional difficulties will arise in creating reasonably homogeneous magnetic fields over such large volumes.

It is this point exactly that ensures the vast majority of NMR experiments occur within a regime in which the RWA is valid. SNR considerations require that the quantizing field be on order 1 T, and it is extraordinarily difficult to construct a coil that could deliver a driving field with an amplitude that is even an appreciable fraction of this size. Thus, the RWA is rarely in a position to be violated for conventional NMR experiments.

It should be noted that one could, of course, relax the requirement for large quantizing field by moving to low temperature – many NMR experiments are

performed at liquid helium temperatures (4 K) or lower – but doing so is often either impossible or counter-productive. For example, research for application to MRIs cannot be performed at cryogenic temperatures, as it would be generally inadvisable to expose human subjects to such conditions (obviously). Protein dynamics, another hot research area in NMR, also cannot be performed at low temperatures, because the fundamental behavior of the system is altered by the change. In many cases, changes of state must be considered as well, since liquid NMR lines are motionally-narrowed [25,26] and thus much easier to observe than broader solid lines, but moving to low temperature would be likely to eliminate this advantage.

This serves to highlight the fact that there is demand within the NMR community, and has been since the method's inception, to identify methods to enhance nuclear polarizations outside of the "brute force" methods of moving to higher field and/or lower temperature. While many methods for artificial polarization enhancement – most with dramatically limited applicability – have emerged over the years, one in particular, spin-exchange optical pumping (SEOP), is central to this work and will be discussed at length in the next section.

1.2 Spin-Exchange Optical Pumping and Hyperpolarized Noble Gases

The basic tenants of spin-exchange optical pumping is that a circularly-polarized beam of photons can transfer angular momentum to an ensemble of atoms through resonant scattering, then this polarization can be transferred, once more, to the nuclei of

neighboring atoms through collisional spin-exchange interactions. This process has a storied history in the field of atomic physics, and additionally has a great deal of utility in NMR, as it has been shown to yield nuclear polarizations on order unity under proper conditions. This section will provide a brief history of the development of the method before moving on to give an overview of the theory that describes the two basic processes at work.

1.2.1 A Brief History of Spin-Exchange Optical Pumping

Optical pumping was pioneered in the famous lab of Alfred Kastler at the École Normale Supérieure in Paris. Along with his first student, Jean Brossel, Kastler extended the spectroscopic work of Rabi to study excited atomic states. Undoubtedly their most influential realization in this field was that it is possible to transfer angular momentum from resonant, circularly polarized light to ground state atoms [27]. Not only did this work constitute the birth of optical pumping, but it was also invaluable to the development of the laser [28] as well as to the precise determination of atomic energy levels [29]. For this work, Kastler would receive the Nobel Prize in Physics in 1966.

Less than a decade after Kastler and Brossel's landmark discovery, another product of Kastler's lab made a breakthrough. Marie-Anne Bouchiat, then working in the lab of Tom Carver at Princeton University, tested the prediction that optically-pumped alkali vapors could transfer their polarization to the nuclei of buffer-gasses through spin-dipole interactions which are strong during collisions [30]. Such a polarization transfer was indeed observed with Rb and ^{3}He, and with that, the field of spin-exchange optical

pumping had been realized.

1.2.2 Optical Pumping: Atomic Polarization Through Resonant Scattering

Optical pumping centers around the transfer of angular momentum from circularly polarized light to ground state atoms [31]. Although the general umbrella of optical pumping includes both *depopulation* and *repopulation optical pumping*, SEOP is based upon depopulation optical pumping, which will therefore be the focus of the following discussion.

Atoms in their ground state will absorb incident photons when the energy of those photons matches that of an available transition to an excited state. Circularly polarized light carries an additional angular momentum selection rule, $\Delta m_f = \pm 1$. Under these selection rules, certain transitions from the ground state will be forbidden, but the processes that govern relaxation will not be held to these same selection rules. Calculation of Clebsch-Gordon coefficients shows [32] that there is a nonzero probability of relaxation into the ground-state sublevel from which excitation transitions are forbidden. Thus, the ground-state sublevels from which transitions are allowed are depopulated by a sufficient intensity of resonant photons, creating a population imbalance in the atomic ensemble. This process is illustrated in Figure 1.3.

Subject to these conditions, the average photon absorption rate can be written as

$$\left\langle \Gamma_{op} \right\rangle = \left(1 - 2\left\langle S_z \right\rangle\right) R_p , \tag{1.14}$$

Where $\langle S_z \rangle$ is the ensemble average of the alkali electron spin and R_p is the optical pumping rate, given as

$$R_p = \int_0^\infty \Phi(\nu)\sigma_{op}(\nu)d\nu \,. \tag{1.15}$$

Here, $\Phi(\nu)$ is the flux of photons incident upon the optical pumping cell per unit frequency, while $\sigma_{op}(\nu)$ is the optical absorption cross section. This highlights the importance of maximizing the overlap of the photon and alkali absorption spectra. While matching the center frequencies of the two spectra is simply a matter of purchasing the correct laser, changing the linewidth of the laser can prove a difficult endeavor, or a pricey one. Instead, one can vary the total buffer gas pressure – typical buffer gases include ^{4}He or N_2 – in the cell to pressure broaden the alkali absorption line such that the linewidth overlap is maximized, thereby maximizing R_p.

One of these buffer gases in particular, N_2, plays a crucial role in increasing the efficiency of the optical pumping process. With sufficiently high pressures of N_2 (≈ 50 Torr at room temperature), collisions between the N_2 molecules and the Rb atoms become a dominant source of relaxation from optically pumped excited states. Of crucial importance is that this process is nonradiative, as the N_2 molecule is capable of absorbing the Rb transition energy into one of its characteristic rotational or vibrational modes [28]. Without this process, the Rb atoms excited by the incident light would radiate an *unpolarized* resonant photon in a random direction upon decaying to the ground state, for which the optical depth inside the cell is much smaller than for polarized photons. Such radiation trapping can dramatically limit the final polarization

achievable in the optical pumping cell.

Most optical pumping experiments are performed at reasonably low field (under 100 G). In this regime, the hyperfine and spin-orbit couplings are strong enough in alkali atoms such that the total angular momentum, $\vec{F} = \vec{J} + \vec{I} + \vec{S}$ is the good quantum number. Here, $\vec{J}$, $\vec{I}$, and $\vec{S}$ are the orbital, nuclear spin, and electron spin angular momenta of the alkali atom, respectively. So, when we construct the rate equations that determine the polarization of the noble gas nuclei, we will treat the alkali atoms in terms of their total angular momentum, $\vec{F}$.

1.2.3 Spin Exchange: Collisional Transfer to Noble Gas Nuclei

Spin exchange between a noble gas atom and an alkali metal atom takes place during collisions between the two species, during which two key terms become important perturbations to the interaction Hamiltonian: spin-exchange and spin-destruction.

Nuclear-electron spin-exchange is the interaction responsible for transferring angular momentum from the alkali atoms to the noble gas nuclei, and can be written as

$$V_{KS} = \alpha \vec{K} \bullet \vec{S}, \tag{1.16}$$

where $\vec{K}$ is the noble gas nuclear spin angular momentum. The dominant contribution to the coupling constant α comes from the Fermi contact term in the hyperfine interaction, which requires there to be some probability of the noble gas nucleus and the alkali electron sitting directly on top of each other. This probability increases dramatically with decreasing internuclear separation between the two colliding atoms.

This constant can be written as

$$\alpha(R) = \frac{8\pi g_s \mu_B \mu_K}{3K} \left|\psi(R)\right|^2 . \tag{1.17}$$

where g_s is the electron spin g-factor, μ_B and μ_K are the moments of the electron and noble gas nucleus, and $\psi(R)$ is the alkali electron wavefunction at the location of the noble gas nucleus. The effective field experienced by the noble gas nucleus from this interaction can be expressed as the classical result from a uniformly magnetized medium, multiplied by an enhancement factor, κ_0, which is specific for the noble gas-alkali combination in the optical pumping cell [33]. Knowledge of this enhancement factor is relevant for the characterization of flow-through polarizers and cell preparation techniques, as it allows for simple polarimetry via NMR measurement of the frequency shift [34].

The spin-rotation interaction also becomes relevant during alkali-noble gas collisions, and is a mechanism of polarization loss. It can be written as,

$$V_{sr} = \gamma_{sr} \vec{N} \bullet \vec{S} \tag{1.18}$$

where $\vec{N}$ is the rotational angular momentum of the two colliding atoms.

Both of these interactions play a crucial role in determining the equilibrium values of the alkali and noble gas nuclear spin angular momenta. To determine these steady state values, one must construct rate equations that incorporate the relevant interactions and express them in terms of how they change the angular momentum expectation values of interest for SEOP.

Under common optical pumping conditions, the alkali and noble gas angular momentum rate equations can be written as [35]

$$\frac{d}{dt}\left\langle F_z \right\rangle = R_p\left(1/2 - \left\langle S_z \right\rangle\right) - \Gamma_{sd}(\gamma_{sd})\left\langle S_z \right\rangle - \frac{n_N}{n_a}\Gamma_{se}(\alpha)\left(\left\langle S_z \right\rangle - \left\langle K_z \right\rangle\right) - \Gamma_a^{ext}\left\langle S_z \right\rangle, \quad (1.19)$$

$$\frac{d}{dt}\left\langle K_z \right\rangle = \Gamma_{se}(\alpha)\left(\left\langle S_z \right\rangle - \left\langle K_z \right\rangle\right) - \Gamma_N^{ext}\left\langle K_z \right\rangle. \quad (1.20)$$

Here, Γ_{sd} and Γ_{se} are the spin destruction and spin exchange rates, respectively, and their dependences on the spin destruction and spin exchange strengths, respectively, have been written explicitly. Additionally, the alkali and noble gas number densities are written as n_a and n_N. Of particular interest are the final terms in the two rate equations, which are added phenonemologically to account for external mechanisms which can cause relaxation of the alkali atoms or noble gas nuclei, such as wall depolarization or magnetic field gradients.

Commonly-used diode-laser arrays can routinely provide sufficient photon flux through the optical pumping cell such that $\left\langle S_z \right\rangle \approx 1/2$ with reasonable spatial homogeneity. We can also set Eq. (1.20) to zero and solve for the steady-state average noble gas nuclear spin

$$\left\langle K_z \right\rangle = \left(\frac{\Gamma_{se}}{\Gamma_{se} + \Gamma_N^{ext}}\right)\left\langle S_z \right\rangle. \quad (1.21)$$

We can see here that a major limiting factor for the noble gas polarization will be these external sources of spin relaxation. If they can be made to be significantly smaller than the spin-exchange rate, then noble gas nuclear polarization can also approach unity, but

will never exceed the alkali polarization. These issues are often discussed in the context of "spin-exchange efficiency" and "photon efficiency" [36].

While low spin densities typically prevent NMR from performed on gas samples, the 5-6 order of magnitude polarization enhancement that results from SEOP more than makes up for these deficiencies. It is also crucial to recognize that this polarization is completely independent of the magnitude of the quantizing field. Thus, practical concerns that prevented exploration of the strong-drive regime in conventional NMR experiments do not apply to NMR on hyperpolarized gases, making them an ideal system with which to explore the rich spin physics therein.

1.3 Strongly-Driven NMR: A No-Approximations Solution to the Two-Level System

As we saw in Section 1.1, the Rabi problem can be solved exactly in the case of a rotating driving field. But, such a field is practically challenging to produce in the lab, so linearly-oscillating fields are typically used in their stead. In the vast majority of cases that arise in NMR, the amplitude of the driving field is much smaller than the quantizing field (i.e., $B_0 >> B_1$), which allows for the rotating wave approximation (RWA) to be made. Inside this limit, the effects of a linearly-oscillating field on the evolution of the two-level system are fundamentally identical to those of a rotating field.

But, once we begin to operate outside this limit, effects from the previously-ignored counter-rotating component can begin to rear their heads. Following the example of Jon H. Shirley [37], this section will derive a method for simple calculation of these higher-

order resonant effects and discuss their application to our system, in particular.

Again, we start here with the Schroedinger equation (with $\hbar = 1$) for a driven two-level system,

$$i\frac{d}{dt}\begin{pmatrix} a_\uparrow \\ a_\downarrow \end{pmatrix} = \begin{pmatrix} E_\uparrow & 2b\cos(\omega t) \\ 2b\cos(\omega t) & E_\downarrow \end{pmatrix}\begin{pmatrix} a_\uparrow \\ a_\downarrow \end{pmatrix}, \tag{1.22}$$

except that, in contrast with our previous examples, now the driving field is of a linearly-oscillating form. The first ingenious realization of Shirley's groundbreaking paper on this topic was that this Hamiltonian is of the general form,

$$i\frac{d}{dt}F(t) = H(t)F(t), \tag{1.23}$$

where $H(t)$, our Hamiltonian, is a Hermitian matrix with elements that are periodic in t.

An equation of this form has a general solution, given by Floquet's theorem as

$$F(t) = \Phi(t)e^{-iQt}, \tag{1.24}$$

where Φ is a matrix of periodic functions of t and Q is a constant diagonal matrix with elements q_a which we will call characteristic exponents. Since $H(t)$ is Hermitian, then it can be shown that $F(t)$ is unitary, which forces the characteristic exponents to be real. We can then write the time evolution operator as

$$U(t;t_0) = F(t)F^{-1}(t_0) = \Phi(t)e^{-iQ(t-t_0)}\Phi(t_0). \tag{1.25}$$

The key step here is to realize that the solution proposed by Floquet's theorem can be expanded as a Fourier series, as the solutions themselves are periodic. We can now

write,

$$F_{\alpha\beta}(t) = \sum_n F_{\alpha\beta}^n e^{in\omega t} e^{-iq_\beta t} \tag{1.26}$$

where $F_{\alpha\beta}$ is now an entry in the matrix solution $F(t)$. For clarity, note that α and β denote matrix elements, while n denotes the component in the Fourier expansion. The Hamiltonian can be expanded similarly,

$$H_{\alpha\beta}(t) = \sum_n H_{\alpha\beta}^n e^{in\omega t} . \tag{1.27}$$

These expressions can be inserted back into the Schrodinger equation and re-arranged to yield a recursion relation to calculate the Fourier coefficients $F_{\alpha\beta}^n$

$$\sum_{\gamma k} \left(H_{\alpha\gamma}^{n-k} + n\omega\delta_{\alpha\gamma}\delta_{kn} \right) F_{\gamma\beta}^k = q_\beta F_{\alpha\beta}^n . \tag{1.28}$$

The operator on the left hand side of Eq. (1.28) is called the Floquet Hamiltonian, and can be rewritten for clarity as

$$\left\langle \alpha n \middle| H_F \middle| \beta m \right\rangle = H_{\alpha\beta}^{n-m} + n\omega\delta_{\alpha\beta}\delta_{nm} . \tag{1.29}$$

We have effectively recast our Hamiltonian in a new basis, which we will call the Floquet basis, in such a way that our previously time-dependent, periodic, 2x2 Hamiltonian has been traded in for a time-independent, infinite matrix. This might seem like a bad trade from the perspective of making useful calculations, but Shirley made the astute observation that, now that our Hamiltonian is time-independent, we can apply methods from time-independent perturbation theory to calculate higher-order excitation terms. Particularly, a method developed by Salwen [38] will prove useful for handling

the Floquet Hamiltonian's infinite dimension. This technique identifies two nearly-degenerate diagonal elements of the Hamiltonian, then constructs a 2x2 matrix with perturbative corrections to its elements which approximate the remainder of the infinite matrix.

$$\begin{bmatrix} \ddots & \vdots & \vdots & \vdots & \vdots & \vdots & \vdots & \vdots & \vdots & \iddots \\ \cdots & E_\downarrow - 2\omega & b & 0 & 0 & 0 & 0 & 0 & 0 & \cdots \\ \cdots & b & E_\uparrow - \omega & 0 & 0 & b & 0 & 0 & 0 & \cdots \\ \cdots & 0 & 0 & E_\downarrow - \omega & b & 0 & 0 & 0 & 0 & \cdots \\ \cdots & 0 & 0 & b & E_\uparrow & 0 & 0 & b & 0 & \cdots \\ \cdots & 0 & b & 0 & 0 & E_\downarrow & b & 0 & 0 & \cdots \\ \cdots & 0 & 0 & 0 & 0 & b & E_\uparrow + \omega & 0 & 0 & \cdots \\ \cdots & 0 & 0 & 0 & b & 0 & 0 & E_\downarrow + \omega & b & \cdots \\ \cdots & 0 & 0 & 0 & 0 & 0 & 0 & b & E_\uparrow + \omega & \cdots \\ \iddots & \vdots & \vdots & \vdots & \vdots & \vdots & \vdots & \vdots & \vdots & \ddots \end{bmatrix} \tag{1.30}$$

Shirley gives, as an example, the 2x2 matrix constructed around the nearly-degenerate entries, $E_\uparrow$ and $E_\downarrow + \hbar\omega$,

$$\hat{H}_2 = \begin{bmatrix} E_\uparrow + \delta_\uparrow & \frac{u}{2} \\ \frac{u}{2} & E_\downarrow + \delta_\downarrow + \hbar\omega \end{bmatrix}, \tag{1.31}$$

where $\delta_\uparrow$, $\delta_\downarrow$, and u represent the aforementioned perturbative corrections. Calculating those corrections for the relevant matrix elements is all that remains to calculate higher-order corrections to the resonance condition, which emerge only inside the strong drive regime.

The first-order correction yields the Bloch-Siegert shift,

$$\Delta\omega = \frac{b^2}{\omega} \ , \tag{1.32}$$

which arises due to the connection of diagonal elements in the Floquet Hamiltonian through the negative frequency, or counter-rotating, component of the linearly-oscillating field. Higher-order shifts can be calculated ad nauseum but, as Shirley points out, the first-order correction to the resonance frequency is sufficient for driving field amplitudes up to approximately one-third the energy splitting. This limit will not be exceeded in our work.

This method can also be applied to nonadjacent diagonal entries in the Floquet Hamiltonian, which will be indirectly connected through intermediate states. This approach yields transition probabilities for multiple quantum transitions, which occur for driving frequencies at odd integer divisions of the energy splitting,

$$\omega_p = \frac{E_\uparrow - E_\downarrow}{2p+1} \, . \tag{1.33}$$

This is perhaps our clearest indication yet that, for strong enough driving fields, the eigenstates of the system are "dressed" by the field, as evidenced by the existence of the virtual intermediate states that must exist in order for these transitions to take place. These are not eigenstates of the two-level system itself, but arise from the interaction of that system with the driving field.

Detailed derivations of the relevant transition probabilities along with further information on Floquet theory can be found in Shirley's thesis [39].

1.4: Longitudinally-Modulated Magnetic Resonance

Although performing conventional NMR experiments in the strong-drive regime tends to be quite difficult, given the fact that large quantizing fields are typically necessary in order to achieve observable signal, interest in understanding the dynamics of this regime has continued to push research into clever ways to access it using ubiquitous systems, like liquid proton NMR. One such effort, which resulted from a collaboration between our group and the group of Dr. Mikhail Raikh, also of the University of Utah, is the application of longitudinally-modulated NMR to studies of the strong-drive regime.

Longitudinal modulation has been a relevant concept in magnetic resonance research since it was initially introduced in the context of rotary saturation by Redfield [14]. The technique has since been utilized further for purposes of rotary saturation and echoes [40,41], and has been expanded for application to adiabatic pulses and cross polarization [42-44] as well as line narrowing techniques [45,46]. But the collaboration of which our group was a part sought to use it for a different purpose – to replicate the strong-drive regime in the rotating frame.

Recall from the discussion of conventional magnetic resonance that the rotating frame transformation is made such that the driving field is static in the xy-plane. If the driving is applied on resonance, i.e., $\omega = \omega_0 = \gamma B_0$, then the z-field is completely transformed away, such that the now-static driving field is the only field left in the rotating frame.

Now consider this exact situation, with the addition of a longitudinal modulation

field, $\overrightarrow{B_2} = B_2 \cos(\omega_m t)\hat{z}$, as illustrated in Figure 1.4. With this addition, in the rotating frame, we would now have the driving field static in the xy-plane and a linearly-oscillating field with frequency ω_m along $\hat{z}$, which is precisely the field orientation (within a $\pi/2$ rotation) that we have in the lab frame for a conventional magnetic resonance experiment, without modulation. Of course, we can now note that the practical restrictions that govern the relative magnitudes of B_0 and B_1 do not apply to the combination of B_1 and B_2, allowing for the exploration of the strong drive regime in the rotating frame dynamics of the modulated magnetic resonance system. In fact, the limit in which $B_2 >> B_1$ can be trivially achieved in this system.

Mathematically, this intuitive picture can be verified by a mapping of a weakly-driven, modulated two-level system onto a strongly-driven two-level system without modulation. This mapping is laid out in detail in [32,47]. In this work, it is observed that higher-order resonance effects can be read out through the envelope of the Rabi oscillations, which are shown experimentally to be sensitive to the relevant parameters of modulation, as shown in Figure 1.5. Chapter 3 will present an extension of this work which analyzes the Rabi oscillation behavior of this system via a phase-averaged Fourier transform when subject to a modulation whose frequency takes on fractional values of the Rabi frequency.

1.5 Summary

This section has laid the groundwork for understanding the two primary experiments discussed in this work. These experiments came about as a result of an interesting confluence of various factors which arose over my time as a graduate student – interest from a close collaborator of the Saam group in the fundamental physics of strongly-driven two-level systems, the obvious overlap of the aforementioned physics to other systems subject to similar conditions, and the expertise of the Saam lab in *both* high-field NMR and low-field MR of hyperpolarized gases.

First, Chapter 2 will describe an experiment in which Rabi oscillations of ^{129}Xe nuclei, hyperpolarized via SEOP, were detected in real-time via an indirect optical detection apparatus, designed and built by members of the Saam group, including myself. Access to these real-time Rabi oscillations allowed for spectroscopic experiments on ^{129}Xe nuclear spins to be performed under drive and at arbitrarily low frequencies, representing a novel approach to spectroscopy on dressed nuclear spin states.

Then, Chapter 3 will discuss an extension of the work from Glenn *et al.* [47], once again performed as a collaboration between our group and Prof. Mikhail Raikh, as well as his graduate student, Yue Zhang. This work builds on the initial exploration of limiting regimes in a longitudinally-modulated magnetic resonance system, by considering cases of *fractional modulation* – cases where the modulation frequency is approximately an integer division of the Rabi frequency – and *slow modulation* – where, as you might have guessed, the modulation frequency is slow compared to the Rabi frequency. To aid in the analysis of these regimes, in which many frequency components

were routinely present in the Rabi oscillation dynamics, we developed a method for analysis in the frequency domain, as opposed to the time domain global fits utilized in Glenn *et al*.

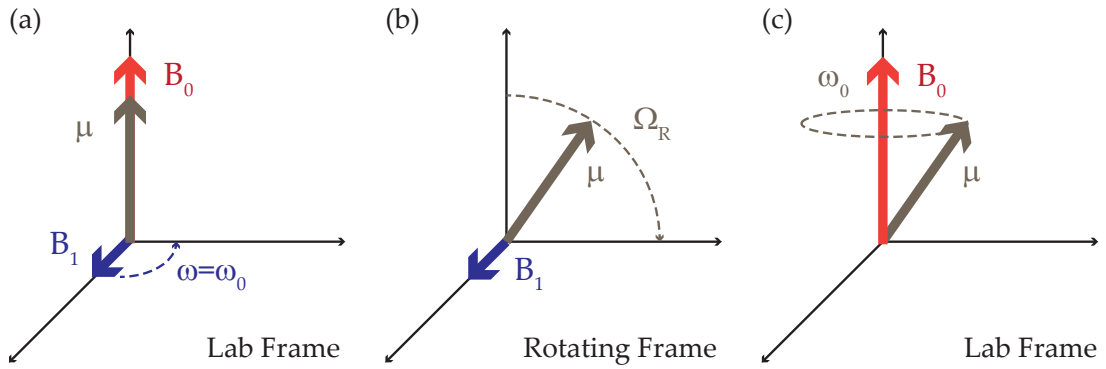

Figure 1.1 Pulsed NMR illustration. Shown here is the progression of a typical pulsed-NMR experiment. Panel (a) shows the moment at which the driving field B_1, which rotates at a frequency $\omega = \omega_0 = \gamma B_0$, is turned on. At this moment, the magnetic moment μ is aligned with the quantizing field B_0, but will be torqued away from this low-energy configuration by the rotating field. (b) Shows the effective field in the rotating frame, in which the driving field B_1 is static along the x-axis. In this frame, the quantizing field is completely transformed away, as the driving field is applied directly on resonance. Since the field and moment are not parallel, the field will exert a nonzero torque on the moment, causing it to nutate away from the z-axis. (c) After the moment has been torqued away from the quantizing axis, B_1 is turned off. At this point, we return to the lab frame, in which there is now only the static field, B_0. The moment will precess about this field at the Larmor frequency ω_0, and this can be detected inductively by a nearby coil.

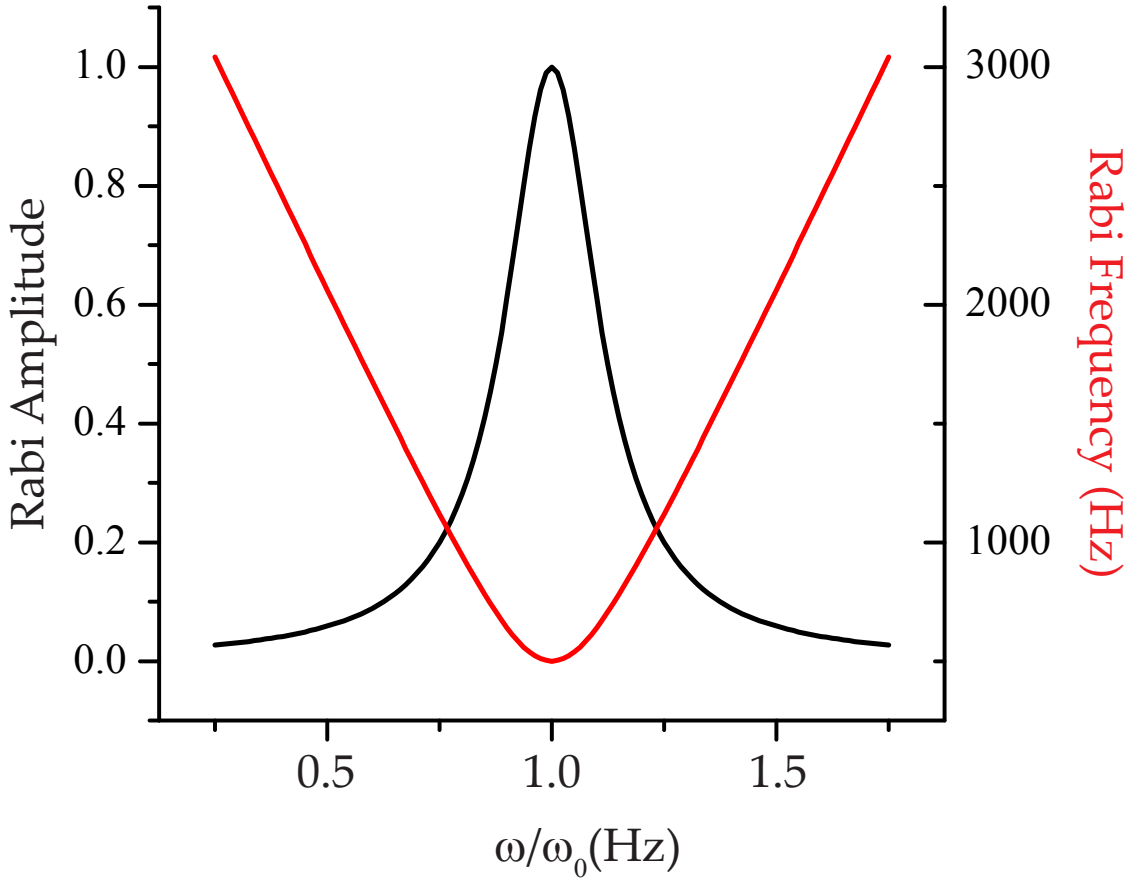

Figure 1.2 Rabi frequency and amplitude vs. driving frequency. The amplitude (black, left axis) and frequency (red, right axis) of Rabi oscillations are plotted as a function of the applied driving frequency, for the ratio $B_1 / B_0 = 1/16$. The amplitude shows a Lorentzian dependence upon the driving frequency, centered on the Larmor frequency ω_0, while the Rabi frequency Ω_R exhibits a hyperbolic shape. These dependences are expected from Rabi's formula, but deviations due to higher-order resonant effects will occur in the strong-drive regime.

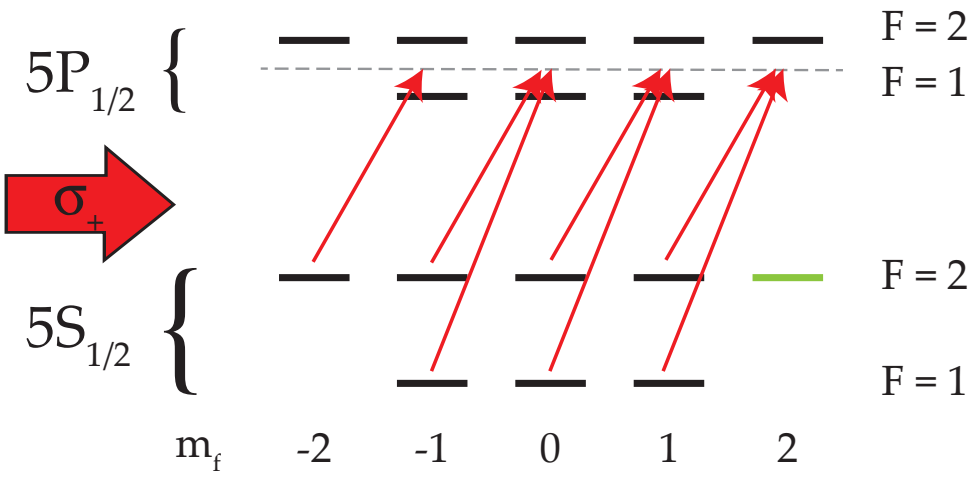

Figure 1.3 ^{87}Rb hyperfine sublevel transitions. Excitation diagram for ^{87}Rb spin states in the ground and first excited states for 795 nm, σ_+ light. The circular polarization of the incident light imposes the selection rule $\Delta m_f = 1$, which prevents any transitions from the ground $m_f = 2$ state, shown here in green. Since the excited atoms have roughly equal probability to decay into any of the available ground states, a population excess will accrue in this state. This process is known as depopulation optical pumping.

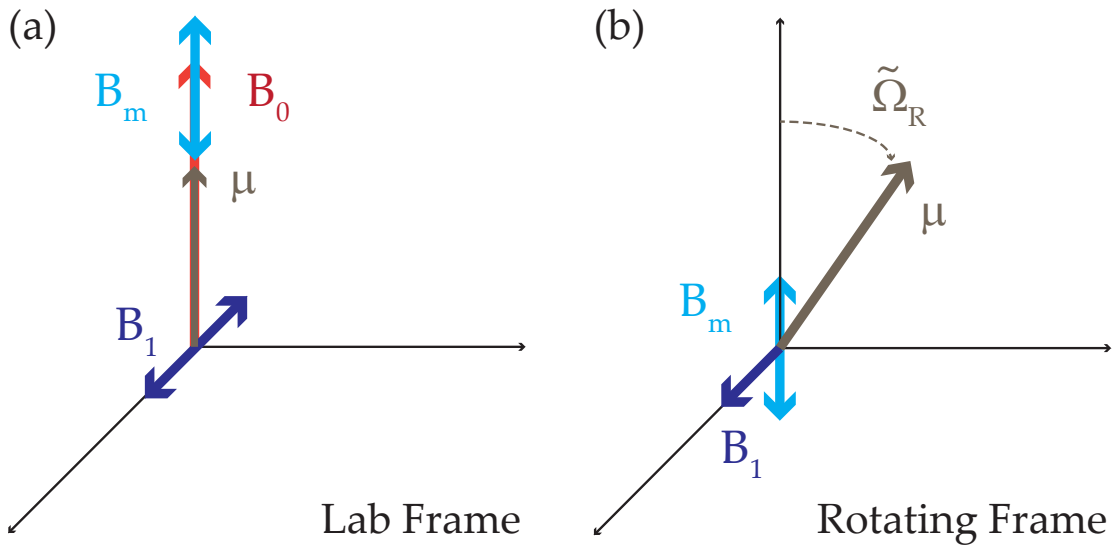

Figure 1.4 Longitudinally-modulated NMR illustration. Shown here is the progression of a pulsed-NMR experiment with an added longitudinal modulation field, $B_m = \varepsilon_m \cos(\omega_m t + \phi)$. (a) In the lab frame, the moment again begins parallel to the quantizing field, but will be torqued away from this orientation by the presence of B_1 but its nutation behavior will be more complex due to the modulation field. (b) In the rotating frame (on resonance), we see that the effective field configuration is similar to that of the lab frame in a pulsed-NMR experiment *without* modulation. The key difference is that, in the rotating frame of the experiment depicted here, B_m can trivially be made on order, or even much larger than, B_1. Such conditions are difficult to achieve in a conventional pulsed-NMR experiment. Effects from the presence of the modulation field, and dependent upon its key parameters, ε_m and ω_m, can be studied by analyzing the Fourier transform of Rabi oscillation data which have been averaged over the modulation phase ϕ, a method which is discussed at length in Chapter 3.

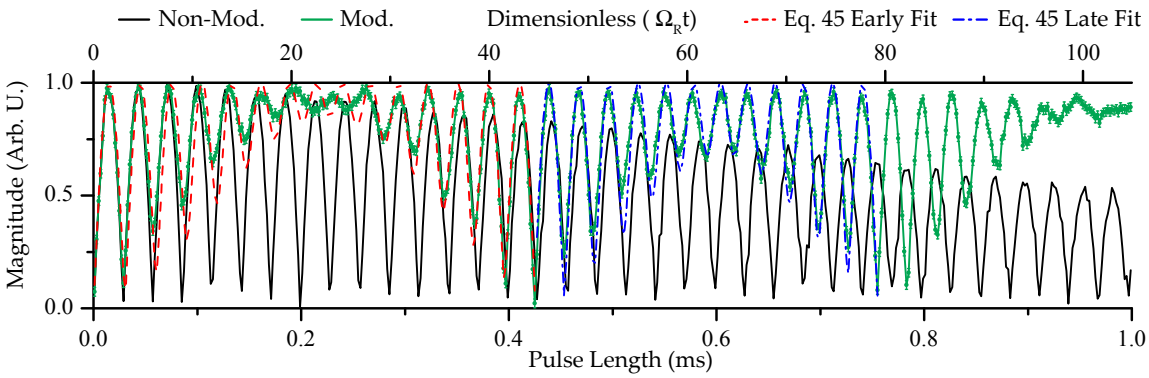

Figure 1.5 Rabi oscillations acquired under weak, resonant modulation. Rabi oscillations acquired from a longitudinally-modulated NMR experiment (green) along with unmodulated Rabi oscillations (black) for comparison [44]. This figure illustrates the "weak-resonant" regime, defined by $\omega_m \approx \Omega_R \gg \varepsilon_m$, and the effects of the modulation can be read out through the envelope of the Rabi oscillations. Note that the amplitude of the Rabi oscillations persist much longer under modulation than in the unmodulated data, and that there are prominent beats in the oscillation envelope, the frequency of which is given by the difference between the modulation frequency and the Rabi frequency. The modulated data are subjected to two fits, an early-time fit (dashed red) and a late-time fit (dashed blue) to account for a drift in the modulation frequency. While a fit to the time domain data is possible in this limiting regime, a different analytical approach will be necessary for longitudinally-modulated NMR experiments which explore outside of the limiting regimes explored in this initial work.
R. Glenn, M. E. Limes, B. Pankovich, B. Saam, and M. E. Raikh, Phys. Rev. B., **87**, 155128 (2013). Reprinted with permission.

1.6 References

[1] D. Halliday, R. Resnick, and J. Walker, *Fundamentals of Physics* (2002).

[2] D. J. Griffiths, *Introduction to Electrodynamics* (1999).

[3] D. J. Griffiths, *Introduction to Quantum Mechanics* (1995).

[4] F. Reif, *Fundamentals of Statistical and Thermal Physics* (1985)

[5] A. Abragam, *Principles of Nuclear Magnetism* (1961)

[6] C.P. Slichter, *Principles of Magnetic Resonance*, 3rd Ed. (1996)

[7] E. Fukushima and S.B.W. Roeder, *Experimental Pulse NMR – A Nuts and Bolts Approach* (1981)

[8] W. Gerlach and O. Stern, Z. Phys., **9**, 349 (1922)

[9] I. I. Rabi, S. Millman, P. Kusch, and J. R. Zacharias, Phys. Rev. **55**, 526 (1939)

[10] F. Bloch, Phys. Rev. **70**, 460 (1946)

[11] E. M. Purcell, H. C. Torrey, and R. V. Pound, Phys. Rev. **69**, 37 (1946)

[12] R. H. Varian, U.S. Patent 2,561,490 (1951)

[13] R. H. Varian, U.S. Patent 3,287,629 (1966)

[14] A. G. Redfield, Phys. Rev. **98**, 1787 (1955)

[15] E. L. Hahn, Phys. Rev., **76**, 145 (1949)

[16] E. L. Hahn, Phys. Rev., **80**, 297. (1950)

[17] E. L. Hahn, Phys. Rev., **80**, 580. (1950)

[18] A. W. Overhauser, Phys. Rev. **92**, 411 (1953)

[19] R. R. Ernst and W. A. Anderson, Rev. Sci. Instrum. **37**, 93 (1966)

[20] F. Bloch, Phys. Rev. **102**, 104 (1956)

[21] J. M. Martinis, S. Nam, J. Aumentado, and C. Urbina, Phys. Rev. Lett. **89**, 117901 (2002)

[22] J.R. Petta *et al*., Science, **309**, 2180 (2005)

[23] Y. O. Dudin, L. Li, F. Bariani, and A. Kuzmich, Nat. Phys., **8**, 790 (2012)

[24] F. Jelezko, T. Gaebel, I. Popa, A. Gruber, and J. Wrachtrup, Phys. Rev. Lett. **92**, (2004)

[25] E.R Andrew and J. Lipofsky, J. Mag. Res., **8**, 217 (1972)

[26] J. L. Bjorkstam, J. Listerud, M. Villa, and C. I. Massara, J. Mag. Res., **65**, 383 (1985)

[27] A. Kastler, J. Phys. Radium **11**, 255 (1950)

[28] W. Happer, Physics Today, **37**, 101 (1984)

[29] A. Kastler, Science, **158**, 214 (1967)

[30] M. A. Bouchiat, T. R. Carver, and C. M. Varnum, Phys. Rev. Lett. **5**, 373 (1960)

[31] W. Happer and W.A. Van Wijngaarden, Hyperfine Interactions, **38** (1987)

[32] M. Limes, Ph.D. Thesis, University of Utah (2014)

[33] M. V. Romalis and G. D. Cates, Phys. Rev. A **58**, 3004 (1998).

[34] Z. L. Ma, E. G. Sorte, and B. Saam, Phys, Rev. Lett., **106**, 193005 (2011)

[35] B. Patton, Ph.D. Thesis, Princeton University (2007)

[36] B. Chann, E. Babcock, L. W. Anderson, and T. G. Walker, Phys. Rev. A **66**, 032703 (2002)

[37] J. H. Shirley, Phys. Rev. **138**, B979

[38] H. Salwen, Phys. Rev. **99**, 1274 (1955).

[39] J. H. Shirley, Thesis, California Institute of Technology (1963)

[40] T. Gullion, Chem. Phys. Lett. **246**, 325 (1995).

[41] A. Pines, M. G. Gibby, and J. S. Waugh, J. Chem. Phys. **59**, 569 (1973).

[42] S. Hediger, B. H. Meier, and R. R. Ernst, Chem. Phys. Lett. **240**, 449 (1995).

[43] M. Garwood and L. DelaBarre, J. Magn. Reson. **153**, 155 (2001).

[44] H. Kessemeier and W.-K. Rhim, Phys. Rev. B **5**, 761 (1972).

[45] H. Hatanaka and N. Tabuchi, J. Magn. Reson. **155**, 119 (2002).

[46] R. W. Mair *et al*., Magn. Reson. Med. **53**, 745 (2005).

[47] R. Glenn, M. E. Limes, B. Pankovich, B. Saam, and M. E. Raikh, Phys. Rev. B., **87**, 155128 (2013)

CHAPTER 2

INDIRECT OPTICAL DETECTION OF HYPERPOLARIZED ^{129}Xe NUCLEAR RABI OSCILLATIONS UNDER STRONG DRIVE

2.1 Introduction

Interest in the dynamics of two-level systems under strong drive has grown significantly with continued advances in two key fields. First, ultrafast atomic spectroscopy [1-4], requires that atomic systems whose excited states have extremely short (~ ns) lifetimes be subjected to strong light fields in order to achieve significant nutation of the state vector away from equilibrium before decay back to the ground state. Second, unconventional magnetic resonance (MR) detection schemes, such as electrically-detected MR (EDMR) and optically-detected MR (ODMR) [5-8], relax the need for strong quantization fields in magnetic resonance experiments by relying on observables other than magnetization to generate the resonance signal.

The strong drive regime is accessed when the ratio of the amplitude of the driving field to the energy splitting between states approaches unity, and is marked by second-order resonance effects such as the Bloch-Seigert shift [9], discussed in Section 1.3. Other

second-order effects include multiphoton transitions [10,11] in which the presense of virtual states allow for transitions to be driven when the excitation frequency takes on fractional values of the energy splitting, and the Autler-Townes effect [12] in which the shapes of absorption and emission spectra are distorted by the driving field. These effects can be accounted for in a dressed state picture, in which the zeroeth-order eigenstates of the system include effects of the driving field. [3,13].

While this regime is rarely accessed in a traditional nuclear magnetic resonance experiment due to the large quantizing fields necessary to achieve observable nuclear spin magnetization, noble gas nuclei hyperpolarized via spin-exchange optical pumping [14] (discussed at length in Section 1.2) can provide an ideal system to explore the strong-drive regime at arbitrarily low frequencies, as the polarization of the nuclear spin ensemble is, in this case, independent of the size of the quantizing field.

The Fermi contact interaction present during collisions between alkali metal (in this case, ^{87}Rb) and noble gas (^{129}Xe) atoms results in a collisionally averaged effective field, given as [15]

$$\delta B_{Rb} = -\frac{8\pi}{3}\kappa_0 \gamma_{Xe} \left[Xe \right] \left\langle \vec{K} \right\rangle \tag{2.1}$$

where δB_{Rb} is the field seen by ^{87}Rb atoms due to ^{129}Xe polarization, γ_{Xe} is the Xe gyromagnetic ratio, $\left[Xe \right]$ is the volume-averaged Rb number density, $\left\langle \vec{K} \right\rangle$ is the volume-averaged expectation value of Xe nuclear spin, and

$$\kappa_0 = \eta^2 \int_0^\infty \left| \psi_0(r) \right|^2 e^{-V(r)/kT} 4\pi r^2 \, dr \tag{2.2}$$

represents a quantum mechanical enhancement over the classical result for the local field due to a uniformly magnetized sphere [16]. Here, $\psi_0(r)$ is the ^{87}Rb electron wavefunction and $V(r)$ is the interatomic potential. The frequency shift of the Rb hyperfine spectrum due to δB_{Rb} has been to detect ^{129}Xe spin resonance [17,18]. However, we expand on the aforementioned works by implementing a frequency-shift-based optically-detected magnetic resonance scheme, which allows for simultaneous NMR excitation and detection of the corresponding Rabi oscillations in real time. Such real-time detection of Rabi oscillations is impossible in a single-coil NMR experiment and difficult in a two-coil experiment due to coupling between excitation and detection coils. The scheme employed here provides a much greater degree of isolation between the rf excitation and optical detection.

Here we present ^{129}Xe nuclear spin Rabi dynamics under drive, observed by monitoring the change in ^{87}Rb spectral intensity at a particular frequency, due to the collisionally-enhanced Fermi contact interaction. We explore the strong-drive regime at low frequency ($\omega_{o,Xe} \leq 31$ kHz) and perform spectroscopy on dressed nuclear spin states. We developed a model for the spectroscopic behavior based on the dressed-state picture and find good agreement with this model, except that we must incorporate an additional term in the Hamiltonian to account for a relaxation-induced frequency shift observed in the data [19-22].

2.2 Experiment

NMR experiments are performed on hyperpolarized ^{129}Xe nuclei with $B_0 \leq 30$ G. The sample is contained inside a spherical Pyrex optical pumping cell, with an inner diameter of $\approx$ 1 cm. These cells contain ≈ 100 mg of naturally-abundant Rb (about 27.8% ^{87}Rb), along with a gas mixture with total room temperature pressure of 2150-2400 Torr, consisting of 25-40 Torr ^{129}Xe, with the remainder consisting of ^{3}He and N_2. Table 2.1 shows the exact contents of all cells used in these experiments. Though variation in the wall relaxation time typically accounts for the major differences in cell performance, changes in cell contents are expected to affect parameters important to optical-pumping, such as the spin-up time [23] and therefore the maximum noble gas polarization, but changes of this nature have negligible impact on this experiment, for reasons which will be outlined below. We also note that spherical cell geometry is chosen specifically such that the through space field from the polarized Rb atomic ensemble is averaged to zero. The pull-off stems from the cell filling process represent a small deviation from a purely spherical geometry, but since they make up such a small percentage of the overall cell volume, any through-space field that results from this deviation is, for the purposes of this experiment, negligible [24].

Figure 2.1 provides an illustration of our experimental apparatus. The cell, along with two excitation coils, is held inside of a Teflon oven with windows along the pump and probe axes. A forced air system, coupled with a temperature controller, is used to maintain an optical pumping temperature of 150° C, which is read via a resistive thermo-couple sensor attached to the cell. Optical pumping experiments are generally

performed at these temperatures to increase $\left[Rb\right]$, which serves to increase the spin-exchange rate, per Eq. (1.15) in which the dependence on the Rb vapor pressure is contained in σ_{op} [25].

A 60 Watt diode-laser array (DLA), tuned to the Rb D_1 resonance (795 nm) and narrowed to ≈ 0.2 nm [26], establishes an optical axis parallel to the quantizing field provided by an ≈ 30 G Helmholtz pair. The direct current (DC) supply powering the coils is actively stabilized by a FET-based control circuit [20]. Two hand-wound excitation coils mounted inside the oven are oriented perpendicular both to this optical axis and to each other, in order to minimize mutual inductive coupling. These coils, both untuned and consisting of two coaxial circular coil winds, will provide driving fields for both the ^{87}Rb and ^{129}Xe. The ^{129}Xe coil operates in the frequency range from 8-30 kHz, and has inner diameter 3.5 cm, coil separation 4.1 cm with 1.5 μH inductance, while the 87Rb coil operates in the frequency range from 5-18 MHz, and has inner diameter of 7 cm, coil separation of 8 cm, with 16.5 nH inductance.

As shown in Figure 2.1, a low-power (~100 mW) Melles Griot probe laser is oriented horizontally transverse to the pump axis and tuned near the Rb D_2 resonance with narrowed excitation linewidth of 0.15 nm. The probe laser is kept 2-3 Å off-resonance to minimize absorption of the probe light by the Rb atoms, but is kept close enough to take advantage of the near-resonant enhancement of Faraday rotation [27,28]. An Edmund Optics 54-520 Si fast photodiode is mounted on an optical table on the opposite side of the cell, also on the transverse axis, and measures the intensity of the probe beam after it

passes through the cell. Since we want to use the photodiode to measure the probe beam's Faraday angle, a linear polarizer, oriented at approximately 45 degrees with respect to the polarization plane of the laser, is mounted between the cell and the photodiode. If Faraday rotation changes the polarization angle of the probe beam as it passes through the optical pumping cell, then it will be observed as a maximal change in intensity at the photodiode. The raw photodiode signal is fed into a Miteq AU-1467 pre-amplifier, with an operating range of 0.01-500 MHz, such that the amplified signal can be fed into our Tecmag Redstone NMR spectrometer [MODEL AND S/N], where it is heterodyned, filtered, further amplified, then digitized for display. The Redstone has two independent transmit channels, which allows for simultaneous excitation of the ^{87}Rb and ^{129}Xe spins. While the Redstone spectrometer is typically designed for use in high field solid state NMR, the transmit channels can be engineered to operate at much lower frequencies (≈ 10 kHz) as is the case for ^{129}Xe excitation in this experiment. Additionally, since we are working at low field, the frequencies for excitation of the electron-like moment of the ^{87}Rb atom fall in the typical band for high field NMR. So, we are here using the Redstone to simultaneously perform EPR and very-low-field NMR.

The Faraday angle accumulated by the probe beam as it passes through the optical pumping cell will depend upon the total Rb magnetization in the cell. If we drive the ^{87}Rb ensemble in the weak limit ($1/\tau_{Rb} \gg \Omega_{R,Rb}$), then a small portion of the total magnetization will persistently precess about the quantizing field. This behavior will result in a small modulation of the Faraday angle of the probe beam. The modulation amplitude depends upon the Rb hyperfine spectral intensity at the Rb driving

frequency. The Faraday modulation occurs at the ^{87}Rb Larmor frequency, which is determined by the total field seen by the ^{87}Rb atoms. This total field consists of both the applied field and a contribution from the local environment. This contribution is dominated by the time-average field due to the collisional Fermi-contact interaction between Rb and Xe atoms, given in Eq. (2.1), which accounts for a substantial shift (≈ 5-10 kHz) when the ^{129}Xe ensemble is hyperpolarized. The direction of this shift is determined by the state into which the Rb spins are pumped, which will inform whether the hyperpolarized Xe nuclear ensemble will point parallel or antiparallel to the quantizing field.

We can utilize the dual-channel capabilities of the Redstone spectrometer to drive the Xe spins with a long NMR pulse while simultaneously driving the Rb ensemble in the weak-drive limit. The nutation of the Xe spins during the pulse yields a sinusoidally-varying contribution to the total field seen by the Rb spins, inducing a modulation in the ^{87}Rb Larmor frequency. This modulation moves the ^{87}Rb hyperfine spectrum back and forth with respect to the fixed Rb driving frequency, which can be read out as a sinusoidal change in the amplitude of the Faraday angle modulation of the probe beam.

The fidelity of the detected Rabi oscillations depends on the size and linearity of $dI_{Rb}/d\omega$, where I_{Rb} is the Rb hyperfine spectral intensity, at the chosen fixed Rb driving frequency, i.e., one would typically operate along the side at about half the height of a strong transition line, as illustrated in Figure 2.2. In this experiment, systematic errors due to deviations from linearity – which would cause the observed Rabi oscillations to deviate from their conventional sinusoidal shape – are avoided by taking the Fourier

transform of the time domain signal, then using the integrated intensity of the peak at the Rabi frequency as a measurement of the oscillation amplitude, and the spectral center of the peak as the oscillation frequency. This avoids the use of fitting routines which assume the oscillations are purely sinusoidal in shape to extract these crucial parameters.

Thus, the ^{129}Xe nuclear Rabi dynamics, encoded in the amplitude of the probe beam modulation, can be read out in real time. One such real-time signal, which consists of the raw photodiode output mixed down to near-DC with the excitation frequency, is shown in Figure 2.3. This represents a dramatic reduction in observation time from the conventional pulse-receive method for plotting Rabi oscillations in NMR experiments, in which Rabi oscillations are measured by tracking the magnitude of the free induction decay (FID) as a function of pulse duration.

Additionally, this method allows for rare access to nuclear spin dynamics *during the excitation pulse*, where the dressed-state picture is applicable, given adequately strong excitation. This access allows us to perform spectroscopic experiments on dressed ^{129}Xe nuclear spin states by measuring the amplitude of the ^{129}Xe Rabi oscillations as a function of the Xe driving frequency, ω_{Xe}.

Coupling between the two driving coils produces an uneven detection baseline, which makes it difficult to measure the Rabi amplitude accurately in the time domain. Instead, the Rabi amplitude is measured as the area underneath the Fourier peak corresponding to Rabi nutation. This area is extracted by apodizing the time-domain signal with a Gaussian decay, then fitting the Fourier peak with the corresponding

Gaussian peak function. Plotting this area as a function of ω_{Xe} yields the excitation spectrum of ^{129}Xe nuclear spins under drive, at frequencies several orders of magnitude lower than those at which NMR is conventionally performed.

The parameter range explored here is limited by the fact that, while the Xe spins are completely unaffected by the presence of the Rb driving field, the Rb spins do not entirely ignore the Xe driving field. Since $\omega_{0,Rb} >> \omega_{Xe}$, the Rb spins follow the linearly-oscillating Xe driving field *adiabatically* which results in an additional amplitude modulation of the photodiode signal at ω_{Xe}. The presence of these peaks can obscure useful analysis of the Rabi peak in the Fourier spectrum, and sets a limit on the ratio of $B_1 : B_0$ that can be explored with this technique.

2.3 Results and Discussion

Rabi's formula, Eq. (1.10), shows that, when performed in the weak-drive limit, the experiments performed here should yield a Lorentzian lineshape, whose width is determined primarily by the strength of the driving field. However, in the dressed-state picture, higher-order resonant effects – particularly the Bloch-Siegert shift, a shift in the resonance due to the presence of the counter-rotating component of the driving field, which depends explicitly on the driving frequency, as shown in Eq. (1.32) – will alter this lineshape. We should also be able to observe these higher-order effects by tracking the ^{129}Xe Rabi frequency $\Omega_{R,Xe}$ as a function of the ^{129}Xe driving frequency ω_{Xe}, whose conventional hyperbolic shape should also be altered in the strong-drive regime.

Also observed is an unequal shift in the positions of the maximum Rabi amplitude and the minimum Rabi frequency, which Rabi's formula predicts should occur at the same driving frequency, $\omega_{Xe} = \omega_{0,Xe}$, and are generally seen as interchangeable indicators of the driving field being directly on-resonance. Higher-order resonance effects that are accounted for within the dressed-state picture can, in fact, shift the position of the resonance, but this shift would be expected to affect the position of the minimum Rabi frequency and the maximum Rabi amplitude equally.

However, nothing in our treatment of the dressed-state picture, this far, has included relaxation. Under certain conditions, relaxation effects can indeed affect relevant experimental quantities, such as the Rabi frequency and amplitude [19-22], so accounting for these effects will be crucial for a full understanding our data.

In general, relaxation in magnetic resonance theory can be accounted for either through Redfield theory [29] or via the Liouville-von Neumann equation in conjunction with the density operator, as such:

$$i\hbar \frac{d\hat{\rho}}{dt} = \left[\hat{H}, \hat{\rho}\right], \tag{2.3}$$

where $\hat{\rho}$ is the density operator and $\hat{H}$ is the Hamiltonian. This formulation provides the time evolution of the density matrix and can account for longitudinal and transverse relaxation, assuming appropriate terms are included in the Hamiltonian. However, once these terms are accounted for, Eq. (2.3) can become a computationally burdensome framework with which to analyze our data. An approximation that retains the crucial physics but allows for more rapid fitting and analysis would be preferable and can be

achieved by including a relaxation term in the diagonal of the two-level Hamiltonian,

$$H_{2^*} = \hbar \begin{pmatrix} 0 & 2\Omega\cos(\omega t) \\ 2\Omega\cos(\omega t) & \omega_0 - i\Gamma_r \end{pmatrix} \tag{2.4}$$

where Γ_r is the relevant relaxation rate. With this addition, the resulting time-dependent Schrodinger equation can be solved exactly inside the RWA, yielding [20]

$$P(t) = \frac{\Omega^2}{\Delta^2 + (\Gamma/2)^2 + \Omega^2}\left[\sin\left(\frac{\Omega_R^{\,*} t}{2}\right)\right] \tag{2.5}$$

where

$$\Omega_R^{\,*} = \sqrt{(\Delta + \Gamma/2)^2 + \Omega^2}\,. \tag{2.6}$$

Note here that the corrections to the position of the maximum Rabi amplitude and the position of the minimum Rabi frequency differ by a term linear in Γ_r, resulting in the separation of these phenomena in frequency for values of Γ_r on order Ω_R. This condition is not typically relevant for NMR, as these quantities are often separated by several orders of magnitude. However, since these experiments are performed at unconventionally low frequencies, these shifts will become relevant to our analysis.

Figure 2.4 shows both the integrated Rabi amplitude and the Rabi frequency, plotted as a function of the Xe driving frequency, ω_{Xe}. Each plot has different values of B_0 and $B_{1,Xe}$, while all other parameters are held constant. The plots are arranged with increasing values of the ratio $B_1 : B_0$. The data in each plot are subjected to global fits, such that both the Rabi amplitude and Rabi frequency are fit according to Eq. (2.5), with

the resonant frequency ω_0 adjusted to reflect the first-order Bloch-Siegert correction

$$\omega_{0,BS} \approx \omega_0 + \Omega_R{}^2 / \omega_{Xe} . \tag{2.7}$$

These fits yield values for ω_0 and Ω_R which are in accord with corroborating measurements, and the values for Γ_r yield order-of-magnitude agreement with observed Rabi oscillation decay times. The fit in Figure 2.4(d) diverges from the observed behavior of the Rabi amplitude at low ω_{Xe}, indicating that unaccounted-for higher-order effects may be present in this regime where $B_1 : B_0 \geq 1/3$, though these deviations certainly cannot be due to our exclusion of the second-order contribution from the Bloch-Siegert effect in our fitting function, as contributions from that term are negligibly small, even for $B_1 : B_0 \sim 1/3$.

2.4 Conclusion

In general, the strong-drive regime is inaccessible in NMR experiments, but spin-exchange optical pumping of noble gas nuclear ensembles creates nuclear spin polarizations that are independent of the magnitude of the applied field. Thus, NMR experiments can be performed on these ensembles at arbitrarily low field, which makes the strong-drive regime accessible. We seek to use this access to perform spectroscopy on dressed nuclear spin states, for use in characterization of the strong-drive regime, and as proof-of-principle for future experimental interest in strongly-driven nuclear spin dynamics.

We have presented spectroscopic data on nuclear spin dressed states, acquired at low frequency (~ kHz) via an indirect optical detection scheme, capable of observing nuclear spin Rabi oscillations in real-time. These experiments are performed on hyperpolarized ^{129}Xe nuclear spins in sealed glass cells along with naturally abundant Rb, ^{3}He, and N_2. By optically probing Rb spins under weak drive, we can encode ^{129}Xe Rabi dynamics into the amplitude of a Rb-precession-induced modulation of the Faraday angle of the probe beam, since ^{129}Xe Rabi nutation will shift the position of the Rb hyperfine spectra due to collisionally enhanced Fermi contact interaction between the two spin species. This allows for mapping of the ^{129}Xe Rabi amplitude and frequency as a function of the frequency of the Xe driving field, effectively performing spectroscopy on nuclear spin states under drive at arbitrarily low frequencies. We also develop a model to fit our data, which incorporates effects the first-order Bloch-Siegert shift – a hallmark of the strong-drive regime – along with a relaxation induced frequency shift rarely seen in NMR experiments, but applicable in the frequency range explored here. Though the ad hoc inclusion of this relaxation term represents a preliminary attempt to account for the unequal shift of the minimum Rabi frequency and maximum Rabi amplitude, we note that fit routines that include this term yield better than order of magnitude agreement with relaxation rates estimated from our time-domain data.

Table 2.1 Cell contents (all values in Torr)

Cell number	Enriched Xe (90% 129)	^{3}He	N_2	Total
203C	39.08	2070.8	43.04	2152.93
204A	37.70	2153.88	44.71	2236.29
204B	22.52	2184.62	45.03	2252.17
204C	37.49	2325.07	48.20	2410.75

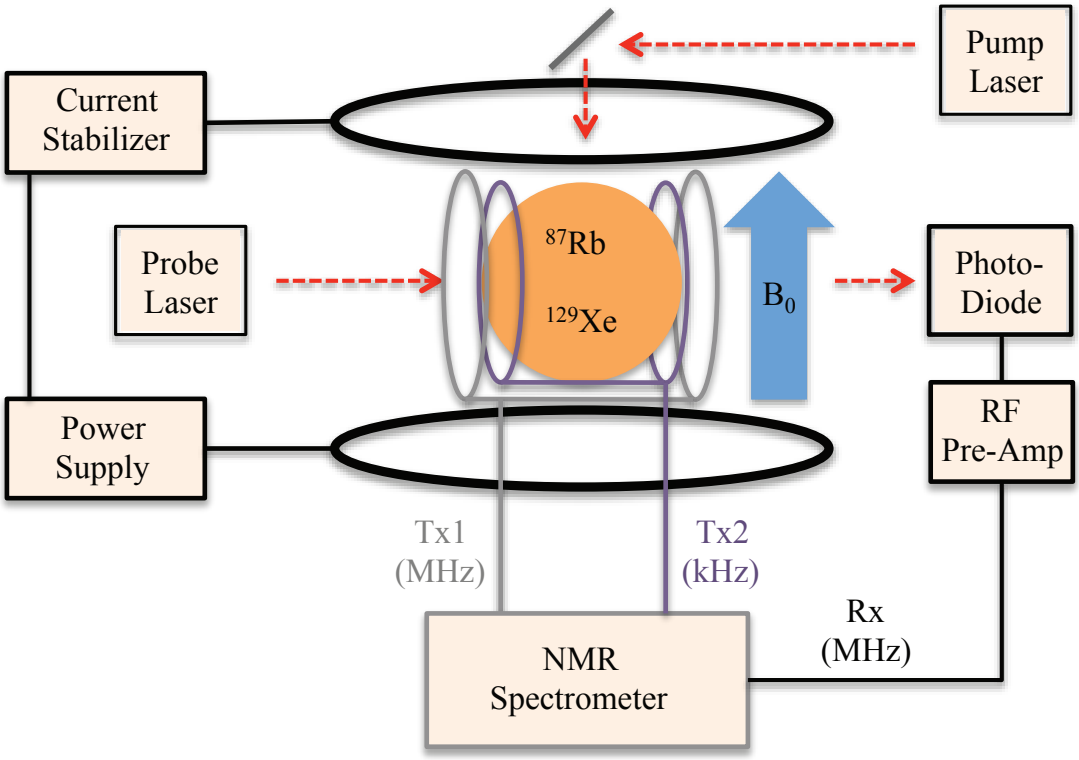

Figure 2.1 Optically-detected ^{129}Xe NMR apparatus. Schematic for indirect optical detection of nuclear Rabi oscillations. ^{87}Rb and ^{129}Xe are contained in a spherical glass cell and simultaneously driven via magnetic excitation. These sinusoidally-varying driving fields are generated by the two transmit channels of a Tecmag Redstone spectrometer. Precession of ^{87}Rb spins under drive modulated the Faraday angle of the probe laser. The amplitude of this modulation is determined by the ^{87}Rb spectral intensity at the Rb excitation frequency, which is, in turn, modulated by the precession of the ^{129}Xe spins, the magnetization of which account for a nonnegligible contribution to the total field experienced by the ^{87}Rb spins. This amplitude modulated signal at the output of the photodiode is then amplified and fed back to Redstone, where it can be mixed with the reference frequency for near-DC detection.

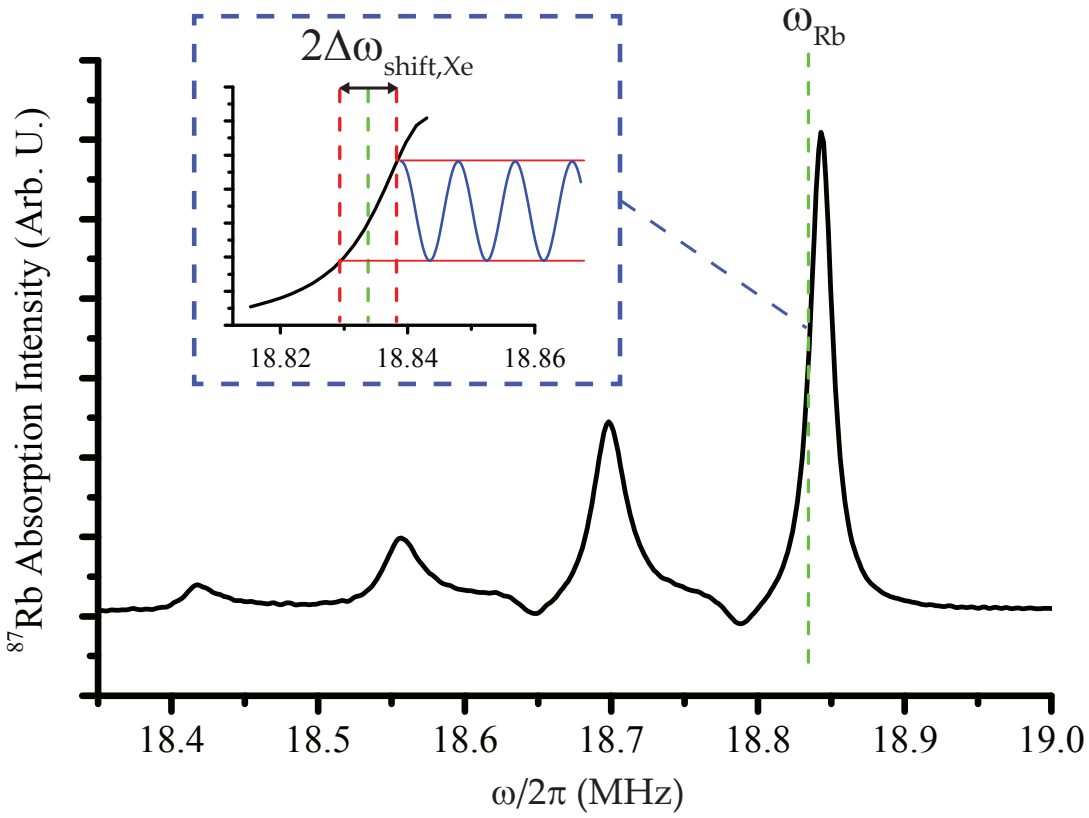

Figure 2.2 ^{87}Rb hyperfine spectrum acquired via optically-detected pulsed-MR. Inset shows the modulation of the ^{87}Rb Larmor frequency due to ^{129}Xe Rabi nutation, which is observed in our optically-detected NMR apparatus as a modulation of the amplitude of the Faraday angle modulation caused by ^{87}Rb precession. This shift in the ^{87}Rb Larmor frequency is large due to the Fermi-contact hyperfine interaction which is relevant during alkali-noble gas collisions. The strength of this interaction is characterized by the scaling coefficient, κ_0 which has been measured to be two orders of magnitude greater for ^{129}Xe-^{87}Rb than for ^{3}He-^{87}Rb [14]. To maximize SNR, ω_{Rb} is chosen where $dI/d\omega$ is maximized, such that we can observe the largest possible change in the Faraday angle modulation amplitude per unit frequency shift due to the nutation of the ^{129}Xe magnetization.

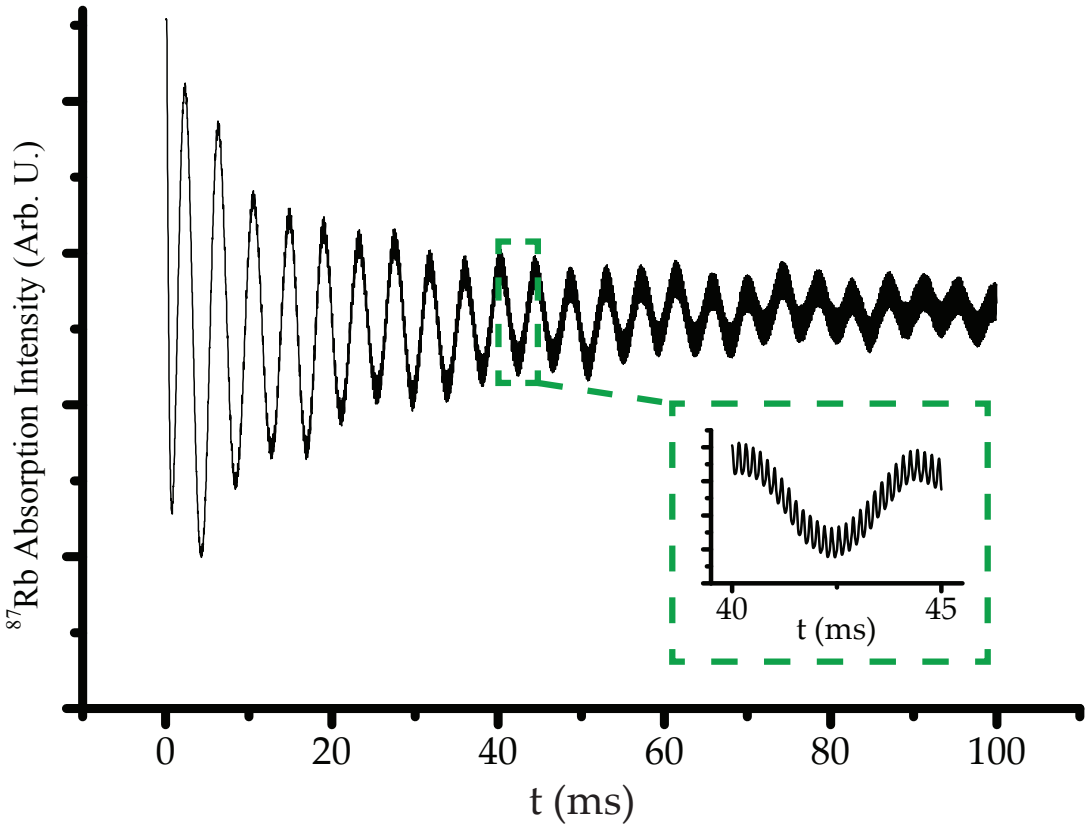

Figure 2.3 Optically-detected ^{129}Xe nuclear Rabi oscillations. ^{129}Xe nuclear spin Rabi oscillations observed in real time via optically-detected EPR of ^{87}Rb hyperfine transitions for $\omega_{0,Xe} \approx 31$ kHz and $\Omega_{R,Xe} \approx 0.25$ kHz. Inset shows adiabatic response of the ^{87}Rb spins to the Xe driving field, which results in a Fourier component at ω_{Xe}.

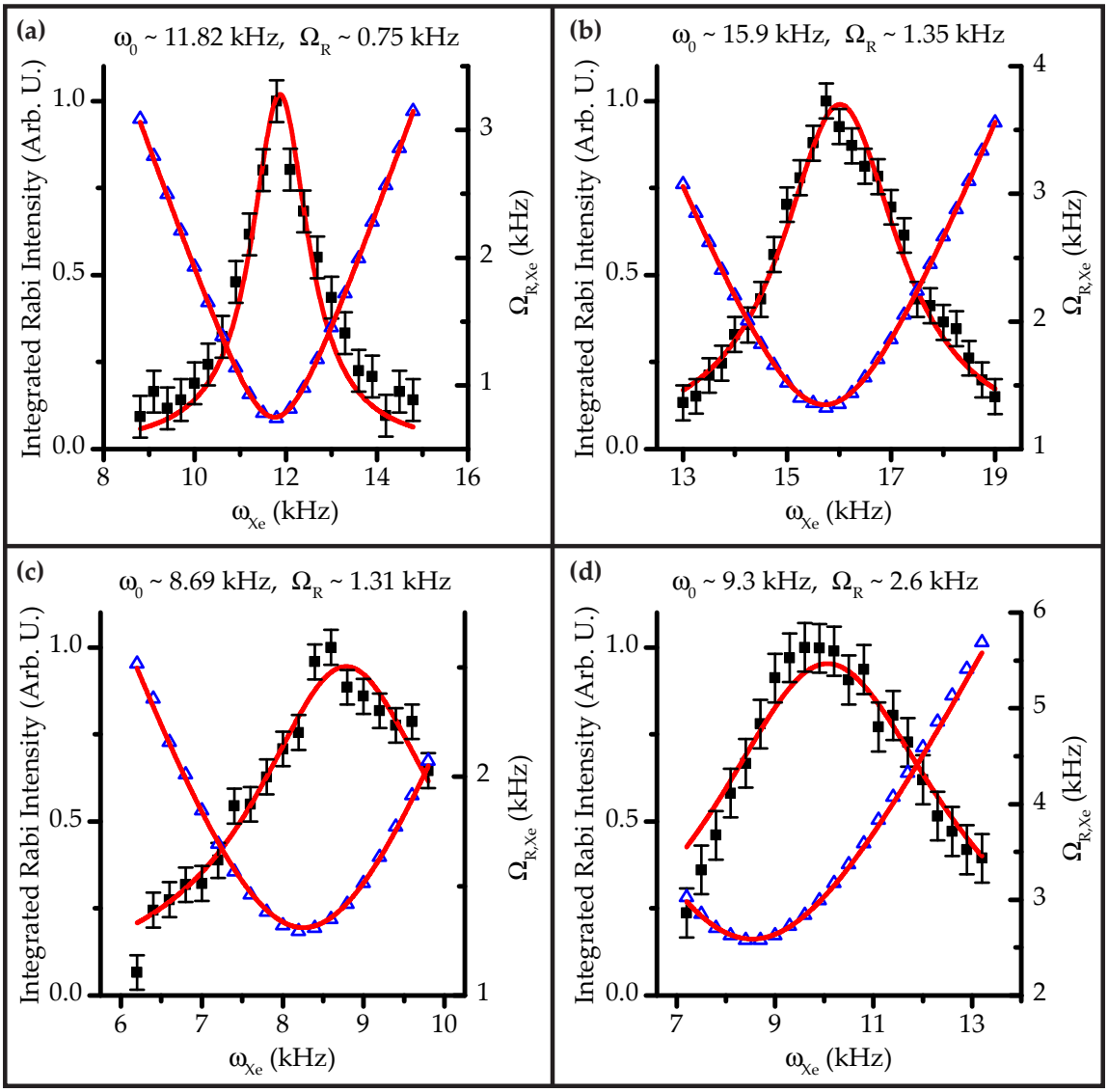

Figure 2.4 Rabi spectroscopy on ^{129}Xe nuclear spin dressed states. Spectroscopic data on ^{129}Xe nuclear spin dressed states, arranged with increasing values of the ratio $B_1 : B_0$. Black, filled-in points (left axes) indicate the integrated intensity of the Fourier peak at $\Omega_{R,Xe}$, while the blue, empty points (right axes) indicates the position of this peak, i.e., the Rabi frequency. Red lines are global fits which share parameters between the fit to the Rabi amplitude and frequency, with additional terms to account for both Bloch-Siegert and relaxation-induced frequency shifts. Instead of This model provides excellent agreement with the data for all except the largest value of $B_1 : B_0$. The inclusion of a relaxation term in the driven two-level Hamiltonian separates the frequencies at which the Rabi amplitude maximum and the Rabi frequency minimum occur.

2.5 References

[1] T. Baumert, M. Grosser, R. Thalweiser, and G. Gerber, Phys. Rev. Lett. **67**, 3753 (1991)

[2] T. Guenther *et al.*, Phys. Rev. Lett. **89**, 057401 (2002)

[3] C. Cohen-Tannoudji and S. Reynaud, J. Phys. B **10**, 345 (1977)

[4] D. Meshulach and Y. Silberberg, Phys. Rev. A **60**, 1287 (1999)

[5] C. Boehme and K. Lips, J. Mater Sci: Mater. Electron. **18**, 285 (2007)

[6] D. R. McCamey, *et al.*, Phys. Rev. B **82**, 125206 (2010)

[7] D. R. McCamey, *et al.*, Nat. Mat., **7,** 723 (2008)

[8] H. Malissa, *et al.*, Science **345**, 1487 (2014)

[9] F. Bloch and A. Siegert, Phys. Rev. **57**, 522 (1940)

[10] M. W. Beijersbergen, R. J. C. Spreeuw, L. Allen, and J. P. Woerdman, Phys. Rev. A **45**, 1810 (1992)

[11] J. Romhányi, G. Burkard, and A. Pályi, Phys. Rev. B **92**, 054422 (2015)

[12] S. H. Autler and C. H. Townes, Phys. Rev. **100**, 703 (1955)

[13] J. H. Shirley, Phys. Rev. **138**, B979

[14] T. G. Walker and W. Happer, Rev. Mod. Phys. **69**, 629 (1997)

[15] Z. L. Ma, E. G. Sorte, and B. Saam, Phys. Rev. Lett. **106**, 193005 (2011)

[16] J. D. Jackson, *Classical Electrodynamics*, 3rd ed. (1998)

[17] I. M. Savukov and M. V. Romalis, Phys. Rev. Lett. **94**, 123001 (2005)

[18] I. M. Savukov, S.-K. Lee, and M. V. Romalis, Nature **442**, 1021 (2006)

[19] W. Demtroder, *Laser Spectroscopy: Basic Concepts and Instrumentation* (1996)

[20] D. Budker, D. F. Kimball, and D. P. DeMille, *Atomic Physics: An Exploration Through Problems and Solutions* (2008)

[21] C. Cohen-Tannoudji, J. Dupont-Roc, and G. Grynberg, *Atom-Photon Interactions: Basic Processes and Applications* (1992)

[22] P. Meystre and M. Sargent III, *Elements of Quantum Optics*, 3rd ed. (1999)

[23] W. Happer and W.A. Van Wijngaarden, Hyperfine Interactions, **38** (1987)

[24] Z. L. Ma, Ph.D. Thesis, University of Utah (2012)

[25] B. Patton, Ph.D. Thesis, Princeton University (2007)

[26] B. Chann, I. Nelson, and T. G. Walker, Opt. Lett., **25** (2000)

[27] L.M.Barkov, D. Melik-Pashayev and M. Zolotorev, Opt. Comm., **70**(6), 467 (1989).

[28] M. G. Kozlov, Opt. Spectrosc. (USSR) **67**(6), 789 (1989)

[29] A. G. Redfield, Phys. Rev. **98**, 1787 (1955)

CHAPTER 3

THE MAGNETIC-RESONANCE SPECTRUM IN A SLOWLY MODULATED LONGITUDINAL MAGNETIC FIELD

The previous chapter detailed an experiment in which the strong-drive regime was accessed by lowering the quantizing field such that it was on order values attainable for the linearly-oscillating driving fields typically utilized in NMR experiments (~ 10 G). However, this method is only applicable in special cases – such as SEOP – where the polarization of our nuclear spin ensemble will not be reduced to undetectable levels by this reduction in the main field – recall Section 1.1.5. If we wish to study the strong drive regime outside of this special case, then we must either seek to engineer coils that can provide linearly-oscillating fields with magnitudes ~ 1 T, or we must get a bit creative.

One such creative solution is to turn to longitudinally-modulated NMR, introduced in Section 1.4. As is laid out in detail in Glenn *et al.* [1], a weakly-driven two-level system *with* longitudinal modulation can be mapped onto a strongly-driven two-level system *without* modulation. As illustrated in Figure 1.4 this mapping can be understood through a transformation to the rotating frame, in which the quantizing field is transformed away and the remaining fields are the linearly-oscillating modulation along the

quantizing axis and the orthogonal, static driving field. A rotation of $\pi/2$ shows this field orientation to be identical to that in the lab frame of a conventional magnetic resonance experiment, with one key difference: the linearly-oscillating field can now be made to be on order, or even much larger than, the static field without technical limitation. In this way, the strongly-driven regime is recreated within the rotating frame, and effects analogous to those seen in conventional strongly-driven systems can be read out through spin dynamics in the rotating frame – namely, Rabi oscillations.

Here, we study Rabi oscillations of protons in water in the presence of longitudinal modulation in both the *fractional* (modulation frequency is an integer division of the Rabi frequency) and *slow* (modulation frequency is slow compared to the Rabi frequency) modulation regimes. These regimes tend to produce Rabi dynamics which are strongly sensitive to the phase of the modulation field and which contain many frequency components, making the time domain analysis utilized in Glenn *et al.* much more difficult to achieve here. In response to this difficulty, a phase-averaged Fourier transform analysis was developed, with which modulation-related effects on the Rabi dynamics could be studied systematically by tracking the position and magnitude of components in the Rabi oscillation Fourier spectrum. Our experimental results provide excellent agreement with theory regarding the dependence of the peak positions on the parameters of modulation. However, the quantitative agreement between theory and experiment regarding the dependence of the Fourier components magnitudes on the parameters of modulation is limited, though the behavior of the peak magnitudes do consistently exhibit key qualitative aspects of the theory.

This chapter is based on a manuscript in preparation, co-authored by myself, Yue Zhang, Mikhail Raikh, and Brian Saam.

3.1 Introduction

In a conventional magnetic resonance experiment, in which a spin in a static magnetic field is subject to a circularly rotating driving field with frequency ω, the equations governing the time-dependence of the two transverse components of the spin vector are given as [2]

$$S_x(t) = \frac{(\omega_0 - \omega)\Omega_R^*}{\Omega_R{}^2}\cos(\omega t)\Big[\cos(\Omega_R t) - 1\Big] - \frac{\Omega_R^*}{\Omega_R}\sin(\omega t)\sin(\Omega_R t) \tag{3.1}$$

$$S_y(t) = \frac{(\omega_0 - \omega)\Omega_R^*}{\Omega_R{}^2}\sin(\omega t)\Big[\cos(\Omega_R t) - 1\Big] - \frac{\Omega_R^*}{\Omega_R}\cos(\omega t)\sin(\Omega_R t) \tag{3.2}$$

where

$$\Omega_R = \sqrt{(\omega - \omega_0)^2 + \Omega_R^{*2}}\,. \tag{3.3}$$

Here ω_0 is the Larmor frequency and $\Omega_R^* = \gamma B_1$ is the Rabi frequency. The Fourier spectrum $F(s)$ associated with the transverse motion of the spins described by Eqs. (3.1) and (3.2), has three components. Relative to ω their positions are:

$$s = 0, \pm\Omega_R \tag{3.4}$$

If we now consider only the positive satellite peak, we can calculate its magnitude as

$$F(\Omega_R) = \frac{\left(\sqrt{\delta^2 + \Omega_R^{*2}} \pm \delta\right)\Omega_R}{4\left(\delta^2 + \Omega_R{}^2\right)}, \tag{3.5}$$

where the sign depends on whether it is the spectrum of S_x or S_y, and

$$\delta = \omega_0 - \omega . \tag{3.6}$$

Now consider an additional modulation field parallel to the driving field, which induces a modulation of the Larmor frequency, given as

$$\omega_0(t) = \omega_0 + \varepsilon_m \cos(\omega_m t + \phi) . \tag{3.7}$$

Here ε_m, ω_m, and ϕ stand for modulation amplitude, modulation frequency, and modulation phase, respectively. The aim of this work is to evaluate the dependence of $F(s)$ on these parameters of modulation both theoretically and experimentally.

In principle, understanding the dependence of Rabi dynamics on the parameters of modulation can be studied in the time domain without Fourier transform and phase averaging. This approach was adopted in ref. [1], and was useful in capturing the strong differences in the response of the Rabi oscillations to modulation in three limiting regimes: $\omega_m >> \Omega_R$, $\omega_m \approx \Omega_R$, and $\omega_m << \Omega_R$. However, this approach is less effective for complex spin dynamics with multiple frequency components, which might be difficult to distinguish in the time domain. Fourier analysis, on the other hand, unveils all harmonics as long as the difference in their positions exceeds the inverse relaxation time.

The characteristics of a driven two-level system are readily manipulated and easily studied with conventional nuclear magnetic resonance (NMR). Early NMR [3-7] was typically performed with a weak cw driving field B_1 and a modulated B_0. In the seminal paper by Redfield [8] field-modulated NMR was used to study Rabi-oscillation

behavior, including rotary saturation and rotary echoes. As pulsed-driving-field methods and superconducting magnets became the norm, modulated-field experiments became less common. In this work we have combined standard pulsed-field methods with the addition of a modest longitudinal modulation field B_m in order to characterize the rich spectrum of Rabi oscillations introduced above and fully characterized in Section 3.4. The experiments are performed on ^{1}H nuclei in a conventional water sample, which provides a robust signal, a single motionally narrowed resonance line whose intensity is easily measured, and the ability to reduce the thermal relaxation time T_1 with a dissolved paramagnetic ion [9]. The reduced T_1 decreases data-acquisition time, allowing us to explore the large parameter space of modulation amplitude, frequency, and phase; detuning from the Zeeman resonance, and the strength of the driving field. We note that our experimental platform can also be used to study the regime of a strongly-driven two-level system, despite the fact that, for both practical and technical reasons, in NMR we almost always have $B_1 << B_0$, i.e., the weak-drive limit. When the strength of our additional modulation field B_m is comparable to or exceeds that of the drive field B_1, then the strongly driven regime can effectively be studied in the rotating frame using the formalism developed in our earlier work [1]. Such systems are realized, for example, in situations where coupled spins are studied by optically probing their singlet/triplet symmetry instead of their magnetization [10-13], as well as in atomic two-level systems, where high-power pulsed lasers can produce the strong electric fields needed to achieve significant nutation of the state vector away from equilibrium before

the system spontaneously decays [14-17].

3.2 Theory Overview

Theory to accompany the experimental work here was initially laid out in ref. [1], in which the mapping of a weakly-driven two-level system *with* modulation onto a *strongly*-driven two-level system *without* modulation was established. This theoretical work is expanded upon by coauthors Yue Zhang and Mikhail Raikh to explore in detail an intermediate regime defined by ω_m smaller than, but still on order, Ω_R. Their findings are summarized in this section.

Within this regime, it is important to distinguish between the weak modulation regime, in which $\varepsilon_m << \Omega_R$, and an intermediate regime in which $\varepsilon_m \sim \Omega_R$. Many of the theoretical predictions made here are valid within the weak modulation regime, and deviations from that regime give rise to additional expansion terms. One of the most important theoretical distinctions presented in this work establishes the regime of applicability for the first set of theoretical predictions given here, noting that this perturbative regime can be exceeded in three ways: with sufficiently large ε_m or δ, or by sufficiently small ω_m. The characteristic equation that determines where this perturbative regime breaks down is given as

$$\omega_m^{**} = \frac{\delta\varepsilon_m}{\Omega_R}. \tag{3.8}$$

At this characteristic frequency, the Fourier components at $s = \tilde{\Omega}_R \pm \omega_m$ are on order

unity. Exceeding this limit causes the peak magnitudes to acquire an *oscillating* character.

Another important feature of the data, justified by theoretical prediction, is that the satellite magnitudes depend strongly upon the phase of modulation, ϕ. As this dependency is difficult to control experimentally, all theoretical predictions are given for Fourier transforms of time domain dynamics, $S_x(t)$ and $S_y(t)$, that have been averaged over this initial phase. It is important to note that this averaging causes the satellites at $s = \Omega_R \pm \omega_m$ to vanish within the perturbative regime.

With these limits in mind, the key findings of the theory, with regard to our analysis of the experimental data, are given here.

(i) Perturbative regime, zero detuning

$$F(\Omega_R) = \frac{1}{4} - \frac{\varepsilon_m{}^2 \omega_m{}^2}{8(\Omega_R{}^2 - \omega_m{}^2)^2}, \tag{3.9}$$

$$F(\omega_m) = \frac{\varepsilon_m{}^2 \omega_m \Omega_R}{8(\Omega_R{}^2 - \omega_m{}^2)^2}, \tag{3.10}$$

$$F(\Omega_R - \omega_m) = F(\Omega_R + \omega_m) = 0. \tag{3.11}$$

(ii) Perturbative regime, finite detuning

$$F(\Omega_R) = \frac{1}{4} - \frac{\varepsilon_m{}^2 \omega_m{}^2}{8(\Omega_R{}^2 - \omega_m{}^2)^2}\left(\omega_m{}^2 + \frac{\delta^2(\Omega_R{}^2 - 2\omega_m{}^2)}{\omega_m{}^2}\right) \tag{3.12}$$

$$F(\omega_m) = \frac{\varepsilon_m{}^2(\omega_m - \delta)\Omega_R}{8(\Omega_R{}^2 - \omega_m{}^2)^2} \tag{3.13}$$

$$F(\Omega_R \pm \omega_m) = \frac{\delta \varepsilon_m{}^2}{16\omega_m(\Omega_R \pm \omega_m)^2}\left(1 \mp \frac{\delta(\Omega_R \pm \omega_m)}{\omega_m \Omega_R}\right) \tag{3.14}$$

(iii) Nonperturbative regime, small ω_m

$$F(\tilde{\Omega}_R + p\omega_m) = \frac{1}{4} J_p^2\left(\frac{\delta\varepsilon_m}{\omega_m \tilde{\Omega}_R}\right) \tag{3.15}$$

(iv) Nonperturbative regime, small ω_m, zero detuning

$$F(p\omega_m) = \frac{p\omega_m}{2\Omega_R} I_p^2\left(\frac{\varepsilon_m}{\tilde{\Omega}_R}\right) \tag{3.16}$$

Here, J_p is the Bessel function of order *p*, and I_p is the corresponding modified Bessel function. Note that in Eq. (3.15), *p* takes on values 0, 1, 2, …, while in Eq. (3.16) *p* takes on values 1, 2, 3, … . Additionally, the modified Rabi frequency $\tilde{\Omega}_R$, which takes into account shifts in the Rabi frequency due to the presence of the longitudinal modulation, is given as

$$\tilde{\Omega}_R = \left(\Omega_R^{*2} + \delta^2 + \frac{\varepsilon_m^{\ 2}}{2}\right)^{1/2} . \tag{3.17}$$

3.3 Experiment

Pulsed-NMR experiments were performed on ^{1}H nuclei in room-temperature water, doped with ≈ 0.1% $CuSO_4$ to reduce the ^{1}H longitudinal relaxation time T_1 to ≈ 100 ms. The cylindrical sample, 5 mm diam by 10 mm long, was contained in Teflon to better match the magnetic susceptibility of the sample, improving the homogeneity of both the main longitudinal field B_0 and the ac drive field $B_1(t) = \left(2\Omega_R / \gamma\right)\cos(\omega t)$. All data were acquired with a Redstone NMR spectrometer (Tecmag, Inc.) with two independent

transmission channels; these were used, respectively, to provide the rf drive field and the audio-frequency modulation field $B_m(t) = (\varepsilon_m / \gamma)\cos(\omega_m t + \phi)$. The rf driving field B_1 was amplified using a model AN8063 (Analogic) 2-kW solid-state amplifier, while the B_m was amplified with a commercial model RA-100 (Alesis) audio amplifier. The initial phase ϕ of the modulation field was controlled by adjusting the delay between the application of B_1 and B_m. The NMR probe consisted of a five-turn, 1-cm-diam, 2.5-cm-long solenoidal coil, series-tuned with a capacitor to resonate at the ^{1}H Larmor frequency ω_0 = 88.8 MHz for B_0 = 2.06 T. A 50-Ω resistor was added in series for impedance matching and to promote a flat (low-Q) frequency response with minimal coupling to the modulation coils. The main magnetic field B_0 was provided by a horizontal-bore (15-cm-diam) superconducting magnet (Oxford Instruments). The modulation coils were a 10-cm-diam Helmholtz pair oriented parallel to B_0 and placed entirely inside the bore of the magnet on either side of the NMR probe and sample; they were similarly tuned to ≈ 10 kHz with a 4-Ω series resistor to match the output impedance of the audio amplifier.

Figure 3.1 shows representative time- and frequency-domain Rabi oscillation data acquired using ^{1}H NMR with no longitudinal field modulation. The time-domain data were acquired point by point, where each point represents the relative amplitude of a free-induction decay (FID) that has been acquired following a single rf nutation pulse of incremented length τ in one of the dual receive channels (in-phase or in-quadrature with a stable carrier reference) of the NMR spectrometer. The amplitude of the driving

field was constant for the duration of the rf pulse, meaning that there was no observable droop in the output of the power amplifier (< 0.5%) over the duration of a 2.0-s rf pulse at 88.8 MHz. Hence, the nutation angle was linearly related to τ. For drive frequencies near resonance ($\delta \approx 0$), the FID amplitudes were measured by recording the signal intensity at a fixed representative time point (beyond the receiver dead time) after the rf pulse. Away from resonance, where the FID oscillates rapidly, the amplitudes were measured by recording the area under their respective Fourier transforms. The frequency-domain data in Figure 3.1 show the expected single peak at the Rabi frequency Ω_R.

Figure 3.2 shows that when the modulation field B_m is present, the time-domain Rabi oscillation data generally become nonsinusoidal, resulting in an additional peak at ω_m and satellite peaks at frequencies $\Omega_R \pm \omega_m$ in the Fourier spectrum. The time- and frequency-domain data for one representative value of the initial modulation phase ϕ are shown in Figure 3.2(a). In general, the magnitudes of the satellite peaks depend strongly on ϕ and quantitative analysis of this spectrum would lead to ambiguous results. In Figure 3.2(b), the data were acquired for 10 equally spaced values of the time delay between the onset of the modulation field and the onset of the rf field, ranging from 0 to $2\pi/\omega_m$, then added together to give phase-averaged time-domain data, which were then Fourier transformed to yield the magnitude spectrum. The needed number of steps between 0 and $2\pi/\omega_m$ in this averaging process was determined empirically by incrementing the number until additional steps no longer changed the appearance of the

spectrum. In comparison to the single-shot spectra with a specific value of ϕ, the positions of the peaks in the phase-averaged spectra remain unchanged, while their relative intensities change dramatically, with the satellite peaks decreasing in magnitude upon averaging. We will thus analyze the evolution of the phase-averaged spectra with respect to modulation amplitude ε_m and detuning δ from the resonance.

3.4 Results and Discussion

The principle result of this paper is that varying the parameters of the longitudinal modulation field results in a theoretically predictable change in the character of the phase- averaged Fourier spectra of Rabi oscillation data, as illustrated in Figures 3.3 - 3.7.

Figure 3.3(a) shows the evolution of the phase-averaged Fourier transform as a function of modulation amplitude ε_m for fixed modulation frequency $\omega_m = \Omega_R / 2$ and in the absence of detuning, $\delta = 0$. Prior to Fourier transformation, the time-domain data for each value of ε_m were baseline-corrected and zero-filled to yield the spectra shown. These results are best compared to the perturbative prediction of Eqs. (3.9, 3.10), where the relevant terms are proportional to $\varepsilon_m{}^2 / \Omega_R{}^2$, which is much less than unity in the entire domain studied. First, we have observed the small shift of the Rabi peak given by Eq. (3.17): a Taylor expansion of Eq. (3.17) shows that the leading fractional correction to Ω_R is $\varepsilon_m{}^2 / 4\Omega_R{}^2$, and that the Rabi peak should shift by about 4% as ε_m increases from 2.1 kHz to 6.8 kHz; the data show the Rabi peak to shift in this interval from 15.2 kHz to 15.8 kHz (3.95%). We next consider the peak intensities: for $\delta = 0$ we have

$F(\omega_m) = \varepsilon_m{}^2 / 9\Omega_R{}^2$ and $F(\Omega_R) = 1/4 - \varepsilon_m{}^2 / 18\Omega_R{}^2$. Thus, we expect a quadratic dependence on ε_m for both peaks, with the ratio of the quadratic coefficients characterizing the evolution of $F(\omega_m)$ and $F(\Omega_R)$ equal to −2. For purposes of analysis, the time-domain data were also exponentially apodized, allowing each of the magnitude peaks to be fit to a Lorenzian. The area under each fitted peak was then computed to yield the plot in Figure 3.3(b), which shows the integrated intensity under each of the two peaks as a function of the modulation amplitude ε_m; the data have been normalized to $F(\Omega_R) = 1$ for $\varepsilon_m = 0$. Data for each peak is well fitted to a quadratic function, with $F(\Omega_R)$ decreasing as $F(\omega_m)$ increases. However, the quadratic coefficient yielded by the fit in each case is about 3 to 4 times larger than expected from Eqs. (3.9, 3.10). Moreover, the ratio of these coefficients is −0.8 instead of −2. Strictly speaking, the theory was developed for $\varepsilon_m << \Omega_R$, which is not well satisfied for our larger values of ε_m. However, we might also expect a concomitant deviation from the expected quadratic behavior for larger ε_m, which was not observed.

We make here a brief remark regarding the line widths of the peaks in Figure 3.3 and later figures. We were able to fit these peaks (with the raw, unapodized time-domain data) well enough to determine that the line widths are proportional to frequency. This suggests that the likely source of the broadening over the frequency domain observed is the inhomogeneity in the rf drive field B_1, the magnitude and frequency of which is essentially the same throughout these experiments. The fact that the peak widths are

unchanged as a function of ε_m in Figure 3.3 argues against inhomogeneity in the modulation field B_m as an additional source of broadening. So, for example, the result of integrating the two sets of peaks in Figure 3.3, whose frequencies differ by a factor of two, changes the ratio of quadratic coefficients by a factor of two compared to what one would calculate by measuring the peak heights alone.

In the next set of measurements, we changed the dependent parameter to the detuning δ from resonance, while keeping the modulation frequency about the same, ω_m = 7.6 kHz, still about half of the Rabi frequency but slightly smaller than for the data in Figure 3.3. The results are shown in Figure 3.4(a) and Figure 3.4(b), respectively, for two different values of ε_m, both of which are significantly larger than the entire range studied in Figure 3.3. Indeed one can treat the two $\delta = 0$ spectra as a continuation of the experiment whose results are shown in Figure 3.3 into the nonperturbative regime, where we first observe $F(\omega_m) \approx F(\tilde{\Omega}_R)$ and finally $F(\omega_m) > F(\tilde{\Omega}_R)$ for the largest value of ω_m. We again observe a shift of the peak near the modified Rabi frequency $\tilde{\Omega}_R$, this time as a function of δ, in accordance with Eq. (3.17). A direct quantitative comparison of the peak-intensity data with theory is nontrivial here, since the regime (nonperturbative but with $\omega_m \sim \tilde{\Omega}_R$) is not one of those well-defined within Eqs. (3.9)–(3.11). However, we note that these data exhibit an important general feature of the theory in this regime that $F(\tilde{\Omega}_R)$ gains intensity and the overall spectrum gains complexity (satellite peaks) as the rf drive field is further detuned from resonance; this is in contrast to conventional

unmodulated NMR, where the peak near the Rabi frequency shifts in a similar way, but $F(\Omega_R)$ essentially disappears with increasing δ. In Figure 3.4(a), where $\varepsilon_m < \Omega_R$, weak satellites emerge only for $\delta \neq 0$ at $s = 2\omega_m$ and $s = \tilde{\Omega}_R - \omega_m$. In Figure 3.4(b), where ε_m actually exceeds Ω_R, these additional peaks are present even for $\delta = 0$ and grow with increased detuning; further peaks emerge at $\tilde{\Omega}_R - 2\omega_m$ and, weakly, at $\tilde{\Omega}_R + \omega_m$. The satellites offset by ω_m from the Rabi frequency are generally predicted by Eq. (10) and should both expected in the limit of a strongly nonperturbative modulation field.

Similar to Figure 3.4, Figure 3.5 also shows the evolution of the Rabi spectrum as a function of the detuning δ; however, in this figure the modulation frequency has been lowered significantly, such that ω_m is small compared to Ω_R. As shown in Section 3.2, the nonperturbative regime can also be attained by choosing $\omega_m << \Omega_R$, even in the case of a weak modulation amplitude. The left panel of Figure 3.5 shows the evolution of the phase-averaged Fourier spectrum as a function of δ, in the nonperturbative regime, with $\omega_m \approx$ 2.5 kHz - small compared to $\tilde{\Omega}_R$. In this regime, Eq. (3.15) predicts the emergence of multiple satellites around $\tilde{\Omega}_R$, with magnitudes given as $F(\tilde{\Omega}_R + p\omega_m) = \frac{1}{4} J_p^2\left(\frac{\delta\varepsilon_m}{\omega_m \tilde{\Omega}_R}\right)$. Although attempts to fit the data to this theoretical prediction were unsuccessful, we point out that the data reflect several qualitative signatures of the theory. First, the Fourier spectra plotted in (a) of Figure 3.5 exhibit peaks at ω_m, $\tilde{\Omega}_R$, $\tilde{\Omega}_R \pm \omega_m$, $\tilde{\Omega}_R \pm 2\omega_m$, and $2\omega_m$, whose appearance and position as a

function of δ are exactly in accord with Eqs. (3.15) and (3.16). Second, while the peak magnitudes do not fit the exact functional dependence predicted in Eq. (3.15), panel (b) of Figure 3.5 clearly shows the nonmonotonic dependence of the peak magnitudes at $\tilde{\Omega}_R$ and $\tilde{\Omega}_R \pm \omega_m$ on δ.

Now, Figure 3.6 shows the evolution of the phase-averaged Fourier spectrum as a function of δ, also in the nonperturbative regime, but further reducing ω_m to ≈ 1 kHz with $\varepsilon_m \approx$ 3.3 kHz. For this value of ω_m, we have not only fulfilled the condition $\omega_m << \Omega_R$, but we have also forced the separation between predicted peak locations to be on order the observed spectral linewidths. As expected, the modulation-induced satellite peaks overlap with the main peak, producing the broadened feature observed near Ω_R. The significant overlap of the satellite peaks prevents quantitative analysis of the development of the peak magnitudes with δ, but it can be observed that the Fourier component at $\tilde{\Omega}_R$ is enhanced with increased δ, as predicted by Eq. (3.15). Once again, the peak locations shift in accordance with Eq. (3.17).

Figure 3.7 again shows the evolution of the phase-averaged Fourier spectrum as a function of δ, with $\omega_m \approx$ 1 kHz, which is still on order the peak width, but with $\varepsilon_m \approx$ 11 kHz, on order Ω_R and dramatically outside the perturbative regime. Thus, the peak at ω_m is dominant for all values of δ. This figure illustrates the point at which the theory described in this work breaks down, as the spectral structure becomes too complex for proper analytic description. However, in the limit of ω_m small and ε_m large, compared

to Ω_R, satellites at $p\omega_m$ should give this complex peak structure definite periodicity $\approx \omega_m$. Such periodicity is roughly observed in the spectra shown in Figure 3.7.

3.5 Conclusion

The strong-drive regime is frequently accessed in myriad driven two-level systems, but conventional NMR is decidedly not one of these systems. The weak nuclear moment requires large quantizing field magnitudes in order to generate observable thermal spin polarizations. The fields are typically much larger than those that can be attained by the linearly-oscillating excitation fields which typically drive transitions in NMR experiments, which ensures that the high-field limit will hold for the vast majority of NMR experiments. However, the addition of a sinusoidally-oscillating modulation parallel to the quantizing field can recreate the conditions of the strong-drive regime. Under such conditions, modulation-related effects – analogous to those observed in other strongly-driven two-level systems – can be read out through the nuclear Rabi oscillations, whose shape can change dramatically based on the parameters of modulation, particularly in certain limiting regimes [1].

We have presented a systematic study of the Fourier spectrum of longitudinally-modulated NMR of protons in water, focusing on the slow modulation regime. Dependences of the position and intensity of peaks in the Fourier spectrum as a function of the parameters of modulation are studied and compared to theoretical prediction. Previous works in longitudinally-modulated NMR applied global fits to time domain

data to assess agreement of data with theory in limiting regimes. However, this work explores the regime of slow modulation, i.e., $\omega_m < \Omega_R$, in which accordance with theory is difficult to determine in the time domain. Instead, we have implemented a phase-averaged Fourier transform, which allows for analysis based upon the magnitudes of peaks in the Fourier spectrum. Though our analysis yields limited quantitative agreement with the theory developed here, our data consistently exhibit key qualitative signatures of the theory. Follow-up work could include an expansion the analysis to regimes outside of slow-modulation and those covered in Glenn *et al.* [1]. A detailed understanding of this regime is crucial to assessing its applicability to more complex magnetic resonance systems, such as EDMR, ODMR, and solid state NMR spectroscopy.

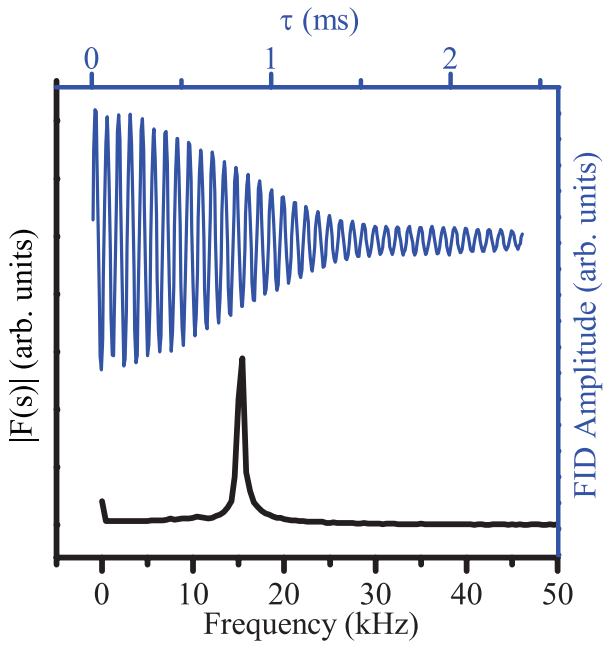

Figure 3.1 ^{1}H Rabi oscillations and accompanying Fourier spectrum. Representative time- and frequency-domain Rabi-oscillation data acquired near resonance ($\delta \approx 0$) for protons in water in an applied magnetic field B_0 = 88.803 MHz with no longitudinal modulation. The time-domain data are acquired point by point, where each point represents the relative amplitude of a free-induction decay (FID) that has been acquired following a single rf nutation pulse of incremented length τ in either the in-phase or in-quadrature receive channel of the NMR spectrometer. The dwell time between points is 8 μs. The coherence time of ≈ 1 ms is dominated by the inhomogeneity of the B_1 field. The magnitude Fourier spectrum shows a single peak at frequency Ω_R = 15.5 kHz, corresponding to B_1 = 3.64 G.

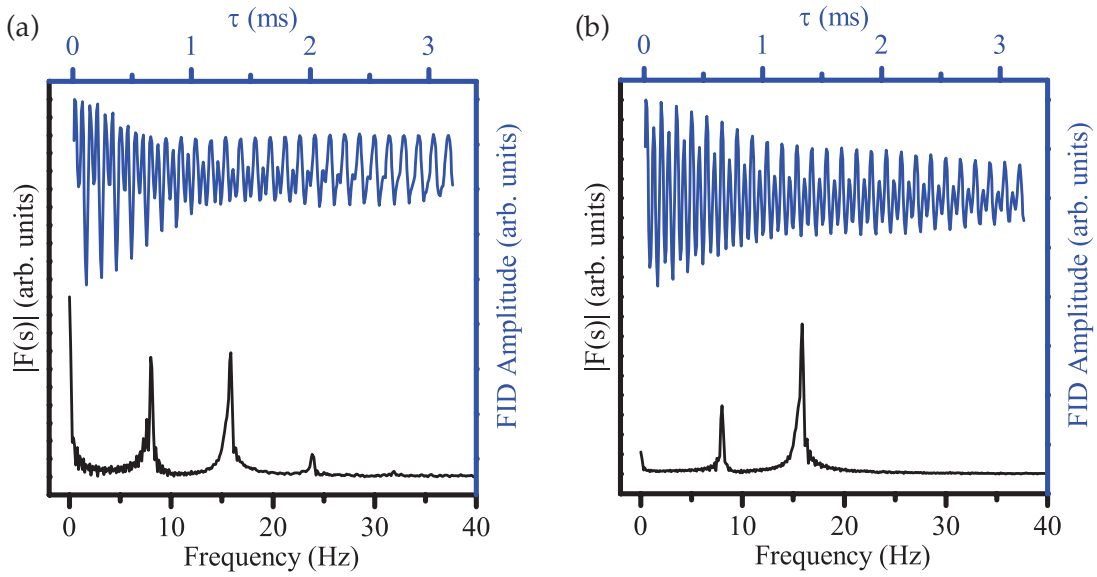

Figure 3.2 Longitudinally-modulated Rabi oscillations with accompanying Fourier spectra. Time- and frequency-domain Rabi-oscillation data for protons in water acquired with a modulation field $B_m \cos(\omega_m t + \phi)$ applied parallel to B_0. The modulation field has amplitude in frequency units of $\varepsilon_m = \gamma B_m \approx$ 4.85 kHz and frequency ω_m = 8.0 kHz; the latter was chosen such that $2\omega_m \approx \Omega_R \approx$ 16 kHz. Panel (a) shows a single acquisition with an arbitrary but fixed phase difference ϕ of the modulation field with respect to the driving field at $\tau = 0$; panel (b) shows the result of averaging 10 acquisitions like those in panel (a), each representing a different value of ϕ, spaced equally between 0 and 2π radians. It is the phase-averaged frequency-domain data that are analyzed in this work, in accordance with the theoretical development in Sec. IV. The single-acquisition Fourier spectrum in panel (a) shows frequency components at Ω_R and ω_m; and satellites at $\Omega_R \pm \omega_m$. According to Eq. (3.11), for near-zero detuning ($\delta \approx 0$) the result of phase averaging in panel (b) is that the satellites disappear, where we note that the choice of $\omega_m \approx \Omega_R / 2$ means that the peak at ω_m is coincident (in both panels) with the position of the left satellite.

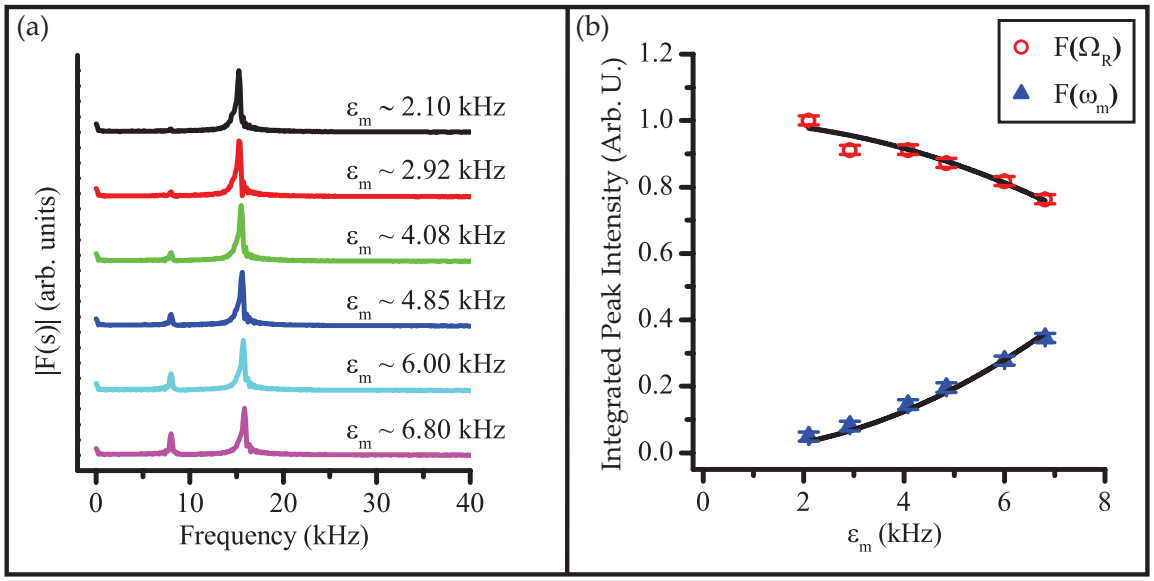

Figure 3.3 Fourier spectral peak magnitudes vs. modulation amplitude. (a) A stacked plot of the Fourier transforms of time-domain Rabi-oscillation data for a range of modulation amplitudes ε_m with fixed ω_m = 8.0 kHz ≈ $\Omega_R/2$ and resonance detuning $\delta \approx 0$. The data shown here have all been averaged over the initial modulation phase ϕ. For these conditions there is a main peak at the Rabi frequency ΩR and a single satellite peak at ω_m. (b) Integrated peak intensities from the spectra in panel (a) plotted as a function of ε_m. In the regime where the modulation field strength is weak enough to satisfy $\varepsilon_m << \Omega_R$, the satellite grows quadratically with ε_m while the main peak decreases quadratically, according to Eqs. (3.9) and (3.10), which also predicts the ratio of the coefficients of the quadratic terms to be −2. We observe the correct qualitative dependences, but they are both stronger than the theory predicts, and the quadratic fits (shown) to our data shown yield a ratio of −0.8 for the quadratic coefficients.

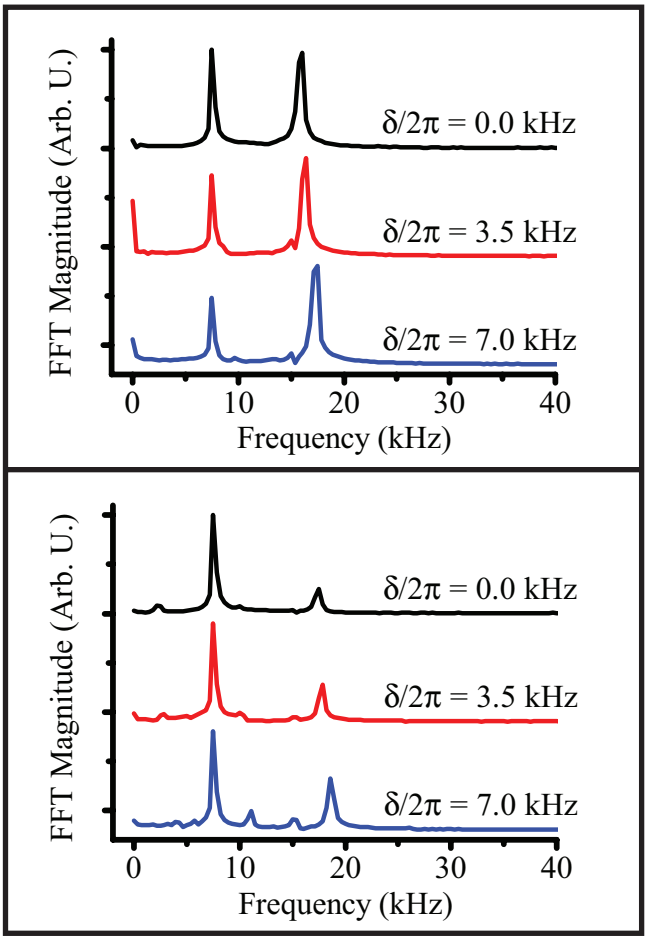

Figure 3.4 Fourier spectra as a function of detuning with fractional modulation. A stacked plot of the Fourier transforms of time-domain Rabi oscillations for three values of the detuning δ from resonance with fixed values of ω_m = 7.6 kHz (slightly lower than in Figure 3.3) and ε_m = 10.24±0.62 kHz (a) and ε_m = 17.82±1.21 kHz (b). These values of ε_m are large enough that the predictions for the peak intensities fall outside the perturbative regime. The spectra in panel (a) show two peaks in nearly the same positions as in the spectra with much lower ω_m shown in Figure 3.3, i.e., at ω_m and at $\tilde{\Omega}_R$, but these now have nearly the same intensity for zero detuning. The peak at $\tilde{\Omega}_R$ is significantly shifted from Ω_R because of the large ε_m; it continues to shift to the right (per Eq. (3.17)) but also becomes more intense with larger detuning δ. The behavior of these two peaks for the still larger value of ε_m in panel (b) is similar, but now additional satellite peaks develop and grow with increasing δ. Contrary to conventional NMR, the resonance near the Rabi frequency gains intensity and the spectrum becomes more complex, developing satellite peaks at $s = 2\omega_m$ and $s = \tilde{\Omega}_R - \omega_m$, as the rf drive field is further detuned from resonance.

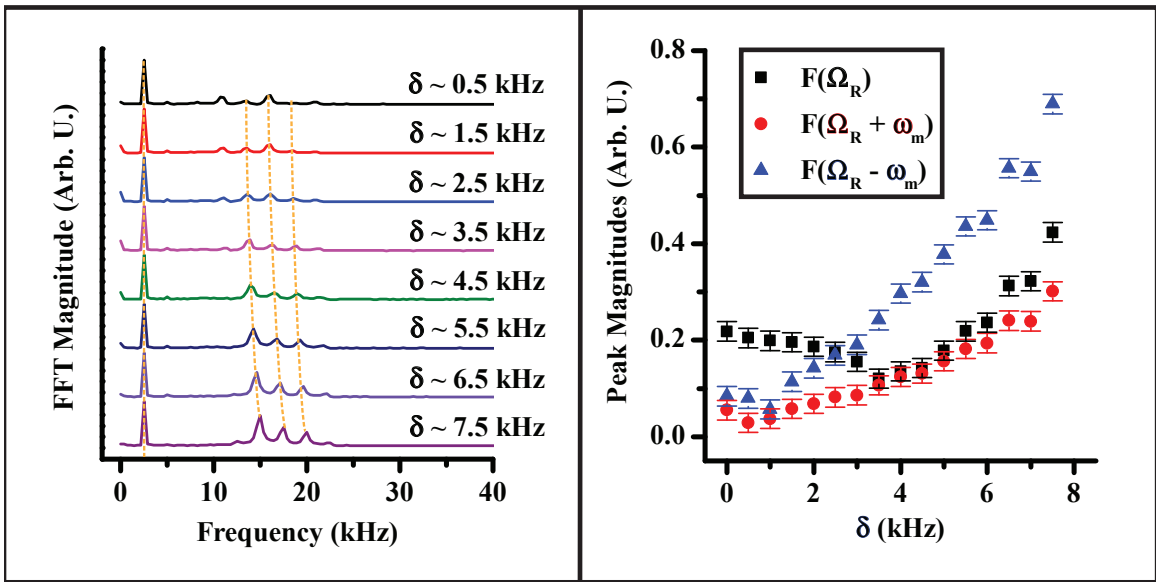

Figure 3.5 Fourier spectra as a function of detuning with strong, slow modulation. (a) A stacked plot of the Fourier transforms of time-domain Rabi oscillations for a range of values of the detuning from resonance δ with fixed values of ω_m = 2.5 kHz and ε_m = 10.74±1.02 kHz. The peak at ω_m is dominant in all spectra, which is expected outside the weak-modulation regime; here, in contrast to Figure 3.3, we do not have $\varepsilon_m << \Omega_R$. Also in contrast to Figure 3.3, ω_m is significantly smaller than $\Omega_R/2$, so that the spectrum exhibits the main peak near Ω_R along with satellite peaks near $\Omega_R \pm p\omega_m$. As expected, these peaks shift in accordance with Eq. (3.17) with increasing δ (b) Peak magnitudes near Ω_R and near $\Omega_R \pm \omega_m$ from the spectra in (a) plotted as a function of δ. This plot illustrates the complex, nonmonotonic dependance of all three peak magnitudes on increasing detuning δ. Though the behavior observed here does not match the functional form predicted in Eq. (3.15), the observed nonmonotonic behavior is in qualitative accord with theoretical expectations for this regime.

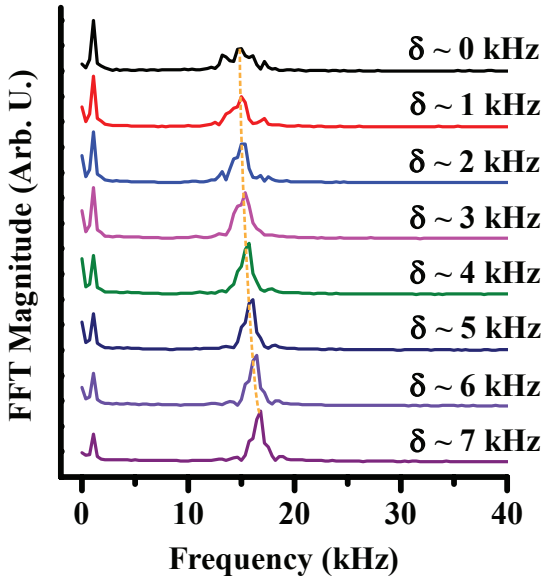

Figure 3.6 Fourier spectra as a function of detuning with weak, slow modulation. A stacked plot of the Fourier transforms of time-domain Rabi oscillations for a range of values of the detuning δ from resonance with fixed values of ω_m = 1.0 kHz and ε_m = 3.30±0.44 kHz. Nonperturbative approach predicts many peaks at $s = \Omega_R \pm p\omega_m$, but since ω_m is on order the observed peak width, these peaks overlap, producing the broadened peak observed near $\tilde{\Omega}_R$. This broadened feature shifts according to Eq. (3.17), and the central feature at $\tilde{\Omega}_R$ grows monotonically with increasing δ. Note, that at $\delta = 0$ we should have no satellites, yet they are present. Despite this particular disagreement with theory, the development of the overlapping satellite peaks is in qualitative accord with theory.

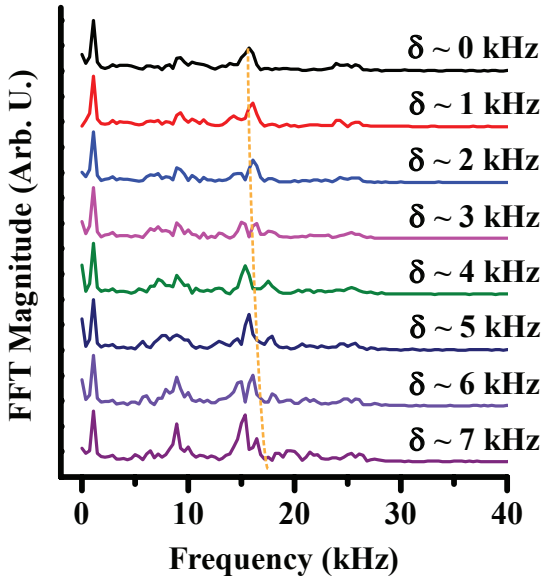

Figure 3.7 Fourier spectra showing breakdown of nonperturbative regime. A stacked plot of the Fourier transforms of time-domain Rabi oscillations for a range of values of the detuning δ from resonance with fixed values of ω_m = 1.0 kHz and ε_m = 10.97±1.47 kHz. With $\omega_m << \Omega_R$ and $\varepsilon_m \sim \Omega_R$, the data presented here are well outside of even the nonperturbative regime described in Subsection G, and the theoretical picture of the development of satellite peaks as a function of δ breaks down. However, well outside the perturbative regime, theory predicts the presence of satellites at $p\omega_m$ and $\Omega_R \pm p\omega_m$ for many values of the integer p. Indeed, the periodicity of the peaks present in the spectra shown here is $\approx \omega_m$.

3.6 References

[1] R. Glenn, M. E. Limes, B. Pankovich, B. Saam, and M. E. Raikh, Phys. Rev. B., **87**, 155128 (2013)

[2] I. I. Rabi, S. Millman, P. Kusch, and J. R. Zacharias, Phys. Rev. **55**, 526 (1939)

[3] F. Bloch, Phys. Rev. **70**, 460 (1946)

[4] E. M. Purcell, H. C. Torrey, and R. V. Pound, Phys. Rev. **69**, 37 (1946)

[5] E. L. Hahn, Phys. Rev., **76**, 145 (1949)

[6] E. L. Hahn, Phys. Rev., **80**, 297. (1950)

[7] E. L. Hahn, Phys. Rev., **80**, 580. (1950)

[8] A. G. Redfield, Phys. Rev. **98**, 1787 (1955)

[9] R. B. Lauffer, Chem. Rev, **87**, 901 (1987)

[10] T. Baumert, M. Grosser, R. Thalweiser, and G. Gerber, Phys. Rev. Lett. **67**, 3753 (1991)

[11] T. Guenther *et al.*, Phys. Rev. Lett. **89**, 057401 (2002)

[12] C. Cohen-Tannoudji and S. Reynaud, J. of Phys. B **10**, 345 (1977)

[13] D. Meshulach and Y. Silberberg, Phys. Rev. A **60**, 1287 (1999)

[14] C. Boehme and K. Lips, J. Mater Sci: Mater. Electron. **18**, 285 (2007)

[15] D. R. McCamey, *et al.*, Phys. Rev. B **82**, 125206 (2010)

[16] D. R. McCamey, *et al.*, Nat. Mat., **7,** 723 (2008)

[17] H. Malissa, *et al.*, Science **345**, 1487 (2014)

CHAPTER 4

CONCLUSION

We have presented the results from two experiments, both of which utilize NMR as a tool with which to explore the fundamental physics of strongly-driven two-level systems.

The experiment detailed in Chapter 1 took advantage of the field-independent polarization of 129Xe, hyperpolarized via spin-exchange optical pumping. NMR experiments on these hyperpolarized nuclear spin ensembles can be performed at arbitrarily low quantizing field magnitudes, at which point the strong-drive regime can be easily accessed. We use a home-built, indirect optical detection apparatus to observe 129Xe Rabi oscillations and perform spectroscopy on nuclear spin states in the strong-drive regime. We use the analytical solution to the driven two-level Hamiltonian, which includes an ad hoc relaxation term and an adjusted Rabi frequency to account for the first-order Bloch-Siegert shift, to provide a fit equation that shows good agreement with our spectroscopic data.

The experiment detailed in Chapter 2 extended the collaboration between the Saam and Raikh groups, centering around the use of longitudinal field modulation in NMR to

recreate the conditions of the strong drive regime in the rotating frame. Under these conditions, modulation-related effects – which are sometimes analogous to effects observed in strongly-driven two-level systems – can be read out in the shape of the resulting Rabi oscillations. We developed a phase-averaged Fourier analysis protocol to systematically explore the slow modulation regime, in which the modulation frequency is slow compared to the Rabi frequency, and consistently confirmed key qualitative features of the theory.

These two experiments were primarily motivated by a desire to show that NMR can be a viable system with which to explore the strong-drive regime – not just as a toy system with which to observe effects common to other strongly-driven two-level systems, but also as a system in which novel research into this increasingly important regime can be performed. Although this regime is most commonly achieved in other two-level systems, such as ultrafast atomic spectroscopy, EDMR/ODMR, and quantum dots, we aimed to show that NMR can also be a playground in which the rich physics of the strong-drive regime can be observed and explained. Potential follow-up experiments could include attempts to observe common effects associated with the strong-drive regime, such multiphoton transitions, either in hyperpolarized 129Xe or longitudinally-modulated NMR, which would provide additional confirmation that the exotic effects associated with dressed quantum states are observable in NMR systems.

APPENDIX

NUCLEAR RELAXATION MEASUREMENTS IN ORGANIC SEMICONDUCTING POLYMERS FOR APPLICATION TO ORGANIC SPINTRONICS

NMR measurements of spin-lattice relaxation of hydrogen nuclei in two prototype organic semiconducting solids, MEH-PPV and DOO-PPV, were carried out for temperatures between 4.2 K and room temperature, and for applied magnetic fields between 1.25 T and 4.7 T. These pi-conjugated polymers are of interest for use as the active semiconducting layer in spintronic devices. They typically exhibit weak spin-orbit coupling, and the interaction with inhomogeneous hyperfine fields generated by the nuclear spins plays a significant, if not dominant, role in the spin coherence and spin relaxation of electronic charge carriers. Our studies were conducted on unbiased bulk material with no photo-illumination. The characteristic ^{1}H longitudinal relaxation times in these materials ranges from hundreds of milliseconds to > 1000 s, and are predominantly nonmonoexponential. We present the data both in terms of a recovery time, $T_{1/2}$, corresponding to 50% recovery of thermal magnetization from saturation and in terms of a "T_1 spectrum" produced via a numerical Laplace transform of the time-

domain data. The evidence best supports relaxation to paramagnetic centers (radicals) mediated by nuclear spin diffusion as the primary mechanism: the observed relaxation is predominantly nonmonoexponential, and a characteristic T_1 minimum as a function of temperature is apparent for both materials somewhere between 77 K and room temperature. The paramagnetic centers may be somewhat-delocalized charge-carrier pairs (i.e., polarons) along the polymer backbone, although the concentration in an unbiased sample (no carrier injection) should be very low. Alternatively, the centers may be localized defects, vacancies, or impurities. Our results may also be used to judge feasibility of Overhauser-type dynamic nuclear polarization from polarized charge carriers or optically pumped exciton states.

This appendix consists of the previously published work [1], co-authored by myself, Mark Limes, Eric Sorte, Valy Vardeny, and Brian Saam.

A.1 Introduction

The inexpensive and versatile nature of pi-conjugated polymer materials coupled with a rich variety of spin-mediated phenomena has made organic spintronics a rapidly growing field in semiconductor physics.[2] Such organic semiconductors (OSECs) generally exhibit weak spin-orbit coupling and correspondingly long electron-spin-coherence lifetimes, which makes them highly suitable for use in devices that rely upon the spin-dependent transport of charge carriers through an active semiconducting layer. However, exceedingly low mobility in OSECs results in spin-transport lengths in the range of tens to hundreds of nanometers, [3] compared to tens of micrometers in more

ordered silicon-based devices.[4] Hence, organic spintronic devices are based on thin-film active layers, generally complicating the fabrication process. Nonetheless, the relative tunability and low cost of the device materials continues to fuel further advances in the field, including the development of spin valves,[5] organic light-emitting diodes (OLEDs),[6] and magnetic sensors. [7]

In light of the relatively weak spin-orbit coupling, it is expected that hyperfine coupling to nuclear spins should play a significant if not dominant role in the spin relaxation of charge carriers, yet key details of how this interaction affects the magneto-transport properties of OSECs remain poorly understood. The coupling of charge carriers to the surrounding nuclear bath has major implications for spin decoherence and the associated characterization of hopping transport inside of OSECs. [8] It is also possible that this coupling could result in an Overhauser-type cross-polarization of the hydrogen nuclei (or of ^{13}C or deuterium in labeled materials). Enhanced nuclear polarization via techniques such as chemically induced dynamic nuclear polarization, (CIDNP) [9] and optically pumped NMR (OPNMR) [10] may also prove feasible. Of the many rate constants involved in such processes, the longitudinal relaxation time T_1 of the nuclei in OSECs is a little studied yet important limiting parameter.

Here, we report NMR spin-lattice relaxation (T_1) measurements of hydrogen made in two prototype OSP materials used in the fabrication of OLEDs and organic spin-valves: [3,11,12] poly[2,5-dioctyloxy-1,4-phenylene-vinylene] (DOO-PPV) and poly[2-methoxy-5-(2-ethylhexyloxy)-p-phenylene vinylene] (MEH-PPV). Chemical structures

for both are given in Figure A.1. These initial experiments were done on bulk material, with no electrical or photo-excitation. We found that the characteristic values of T_1 vary widely, from hundreds of milliseconds to thousands of seconds, depending on applied magnetic field and temperature. Additionally, we found that the relaxation behavior in many instances is significantly nonmonoexponetial, leading us to conclude that spin diffusion to paramagnetic centers is likely the dominant relaxation mechanism. These centers may be actual material impurities but could also be localized charge carriers responsible for the conducting behavior in OSP devices. Given this complexity and following Fukushima and Uehling [13], we have recorded $T_{1/2}$, the time for an initially unpolarized sample to return to half of its equilibrium value; the results for various applied magnetic fields and temperatures are shown in Table A.1. We note here that our T_1 measurements are all of this "saturation-recovery" variety. In Section A.3, we provide a more detailed characterization of the relaxation curves with a Laplace-transform approach, which shows the relative intensities of different exponential components in each case.

A.2 Theory

In broad terms, the possible relaxation mechanisms for spin-1/2 nuclei, for which there can only be magnetic (i.e., no quadrupolar) interactions, in an OSEC are relatively limited. Nuclei in semiconducting materials are generally subject to relaxation via interactions with thermally generated (unpaired-spin) charge carriers in the conduction

band. [14,15] However, this mechanism is utterly negligible in undoped conventional semiconductors, where the equilibrium density of charge carriers is on order $10^{12} - 10^{13}$ cm^3. The band gap in OSEC materials is ≈ 2 eV; large enough that, even at room temperature, the equilibrium concentration of charge carriers should be similarly small. (We return later to the question of the nature and density of charge carriers in OSECs in connection with the mechanism of relaxation to paramagnetic centers.) Another known mechanism is the spin-rotation coupling between moving electrons and the nucleus, modulated by Raman phonon scattering. [16,17] This mechanism is particularly weak for low-Z materials (it has been studied, for example, in solid ^{129}Xe [18] and ^{207}Pb salts [19]) and at low temperatures, where phonons are frozen out. Indeed, there is a characteristic quadratic dependence (as per phonon occupation number) of $1/T_1$ on temperature, which is not observed anywhere in our data. This leaves the interaction of nuclear spins with paramagnetic centers (radicals) as the only other known mechanism. Nuclear spins closer to these centers can undergo direct dipole-dipole cross relaxation, leading to polarization gradients along which spin angular momentum from more distant spins can flow diffusively. Such spin diffusion is mediated by mutual spin flips among nearest-neighbor nuclei, which occur on the time scale of the nuclear-spin T_2. [20] This relaxation mechanism has been observed in both insulating [13,27] and semiconducting [21] solid-state systems and is characterized by the equation: [13,20]

$$\dot{M}(r,t) = D\nabla^2 M(r,t) - \frac{C}{r^6} M(r,t) \qquad \text{(A.1)}$$

where M is the fractional magnetization difference from equilibrium magnetization, D

is the spin-diffusion coefficient, and C is the dipolar-coupling coefficient. An angular dependence in C, arising from the orientation of the applied field B_0 relative to the line connecting the paramagnetic center to the nucleus, can usually be averaged away for a polycrystalline or disordered sample, so that one obtains: [22]

$$\bar{C} = \frac{2}{5}\left(\hbar\gamma_S\gamma_I\right)^2 S\left(S+1\right)\left[\frac{\tau_c}{1+\omega_I{}^2\tau_c{}^2}\right], \tag{A.2}$$

where S and I refer respectively to the spins of the paramagnetic center and the nucleus, γ is the gyromagnetic ratio, $\omega_I = \gamma_I B_0$ is the nuclear Larmor frequency, and τ_C is the correlation time for the interaction, taken here to be the longitudinal relaxation time of the paramagnetic center.

Equation (A.1) is not generally solvable analytically. Limiting regimes have been identified, [26–28] under the assumption that the paramagnetic centers are dilute enough that each nucleus is affected by only one such center, by comparing two characteristic distances. Within the diffusion-barrier radius b, one assumes that the local field surrounding each nucleus is so strongly shifted by the presence of the nearby paramagnetic center that it is completely removed from the magnetic resonance line and cannot be detected by NMR. Furthermore, nuclei within the diffusion-barrier radius cannot exchange energy with nuclei outside the barrier radius via mutual spin flips. In the case where the nuclear-spin $T_2 >> \tau_C$, we can estimate b by comparing the thermal-equilibrium ensemble magnetic moment $\mu_S(\mu_S B_0 / kT)$ of the paramagnetic centers to μ_I [28]:

$$b = a\left(\frac{\mu_s^{\,2} B_0}{\mu_I kT}\right)^{1/3} \tag{A.3}$$

where a is the lattice parameter, k is the Boltzmann constant, and T is absolute temperature. The other characteristic distance in the problem is the pseudopotential radius ρ, roughly the maximum distance from a given paramagnetic center at which the center can relax nuclei through the direct dipole-dipole interaction described by Eq. (A.2). It can be expressed as: [13]

$$\rho = 0.68\left(\frac{C}{D}\right)^{1/4} \tag{A.4}$$

In the "fast-diffusion" regime of $\rho << b$, relaxation is limited by $1/\tau_c$, the rate at which the paramagnetic centers leak angular momentum to the lattice. In this regime, spin diffusion is rapid enough to equilibrate the sample on time scales short compared to the relaxation time, and the sample is well-characterized at all times by a single spin temperature. As a result, one expects monoexponential behavior to characterize the entire approach to equilibrium from an initial unpolarized state with a characteristic rate is given by: [27]

$$\frac{1}{T_{1,f}} = \frac{4\pi}{3}\frac{NC}{b^3}, \tag{A.5}$$

where N is the concentration of paramagnetic centers. In the "diffusion-limited" regime, $\rho >> b$, diffusion is slow enough that significant gradients in the polarization develop during the approach to equilibrium. The presence of such gradients means that the sample cannot be described by a single spin-temperature, and the corresponding spin-

lattice relaxation exhibits multi-exponential behavior corresponding to the multimode spin-diffusion given by Eq. (A.1). The late-time rate (slowest diffusion mode) is given by [26,28]

$$\frac{1}{T_{1,s}} = \frac{17}{2} N\left(CD\right)^{1/4}, \tag{A.6}$$

where we emphasize that Eqs. (A.5) and (A.6) are valid in low-concentration limit, i.e., $\rho << R$, where R is the mean distance between paramagnetic centers. Fukushima and Uehling [13] treat the more general case of larger values of N. For some very short time t, spin-diffusion cannot occur because significant polarization gradients have not yet developed in the sample. Blumberg [27] first formulated the expression for magnetization recovery in this regime:

$$M(t) = 1 - \frac{4}{3}\pi^{3/2} N C^{1/2} t^{1/2}, \tag{A.7}$$

which is valid for $t < C^{1/2} D^{-3/2}$ or, equivalently, when the characteristic spin-diffusion distance is shorter than the characteristic distance over which the dipolar field from the paramagnetic center falls off. The $T_{1/2}$ dependence might be considered an indicator for the impurity-relaxation mechanism; however, such a dependence is not easily distinguishable from a simple exponential dependence over the range of times for which it is supposed to be valid. [13] Moreover, in saturation-recovery experiments, the earliest time points have the lowest SNR.

The magnetic-decoupling factor in square brackets in Eq. (A.2) gives rise in the usual way [23] in both regimes to a minimum T_1 value when $\omega_I \tau_C = 1$, i.e., when the Larmor

period is equal to the relaxation time of the paramagnetic center. Thus, in the high-field limit $\omega_I \tau_C >> 1$, $T_1 \propto B_0^{\,2}$ in the fast diffusion regime and $T_1 \propto B_0^{\,1/2}$ in the diffusion-limited regime. In principle, transitions between these regimes can thus be studied by measuring T_1 as a function of temperature and applied field.

Beyond simply recording the $T_{1/2}$ times in Table A.1, we provide a more general characterization of longitudinal relaxation for these materials by implementing a Laplace transformation scheme to an effective T_1-space. The general form of the Laplace transform is:

$$F(s) = \int_0^\infty e^{-st} f(t)\, dt \,. \tag{A.8}$$

Now, if we let *f(t)* represent the recovery of the sample magnetization as a function of time toward its thermal equilibrium value from $f(0) = 0$, and $s = 1/T_1$, we thus obtain a spectrum of T_1 values from the time-domain relaxation data f(t). Representative time-domain data and corresponding T_1 spectra are shown in Figure A.2 for (a) monoexponential and (b) multiexponential decays.

A.3 Experiment

MEH-PPV was purchased as product number ADS100RE (American Dye Source). DOO- PPV was synthesized in house. Both of these materials were ground into a powder, then stored in 2 cm length by 5 mm diameter pyrex cylindrical NMR sample containers, sealed with teflon plugs. Pulsed-NMR experiments were performed on the

DOO-PPV sample over the course of two years, whereas the experiments performed on the MEH-PPV sample spanned six months. The sealed sample containers helped to slow effects of degradation due to oxygen exposure.

All data were acquired with a Redstone (Tecmag) NMR spectrometer and various home- built tunable probes with 50-Ω impedance, resonant at the Larmor frequency $\omega_0 = \gamma_p B_0$, where the ^{1}H gyromagnetic ratio γ_p = 2π(42.58 MHz/T), and the values of B_0 were 4.7, 2.5, and 1.25 T (see Table A.1). A conventional capacitively-tapped probe design was used at 21 and 53 MHz, and a high-frequency design [24] was used at 85 and 200 MHz. The RF power amplifier, model BT-02000-AlphaSA-T (Tomco), operated between 20-500 W (1-25% of maximum output power). The longitudinal relaxation time T1 of 1H in MEH-PPV and DOO-PPV was measured using the saturation-recovery method: an initial series of hard pulses to destroy any longitudinal magnetization, a variable wait time, τ, and a final read pulse to project some fixed fraction of the recovered magnetization into the transverse plane and record the intensity of the resulting free-induction decay (FID). The saturation comb consisted of 10-50 1-μs pulses separated by a time $T_2 \ll t_{sep} \ll T_1$, typically ≈ 5 ms. In general, the saturation comb preceded each time point in a T_1 measurement and was followed by a π/2 read pulse to maximize the signal from the recovered magnetization. However, in some cases where SNR allowed, the saturation comb was implemented once at the beginning of the entire T_1 measurement, and a low-flip-angle (< 1°) read pulse was used at successive time points in the recovery, significantly decreasing measurement time for many of the

longer T_1 measurements.

All experiments were performed in a vertical wide-bore (89 mm) superconducting magnet (Oxford), for which the field was adjusted down from its maximum (8.0 T) to each of the three measurement fields listed in Table A.1, and in a model MD3A variable-temperature cryostat (Oxford) designed to fit inside the magnet bore. A Cernox (Lakeshore) temperature sensor mounted at the dewar's heat exchanger was used to monitor and control the temperature between 4 K and 77 K. For measurements 77 K and higher, the dewar was first cooled to 77 K and then allowed to drift slowly back towards room temperature. This drift could be maintained ≤ 0.1 K/min and never exceeded a total of 2 K over the course of a T_1 measurement.

Results across the accessible values of applied field and temperature are shown for both MEH-PPV and DOO-PPV in Figure A.3. For the highest temperatures and lowest applied fields, the large dipolar line width (corresponding to $T_2 \leq 20$ μs) led to relatively low SNR, which precluded reliable measurement of T_1. In most cases, the time-domain data are highly nonmonoexponential. For better characterization of these data, we implemented the CONTIN algorithm [25] for a numerical discrete Laplace transformation to a normalized relaxation spectrum, where the intensity at each value of time on the horizontal axis indicates the relative weight of that T_1 component in an assumed multiexponential decay. We note that the uniform width of the spectral peaks is related to finite sampling and does not appear to carry any physical significance. A similar width is generated from the transform of an ideal monoexponential decay and

shows no appreciable dependence on artificially added noise. We treat the transformed data as only a number and intensity of discrete characteristic decay times as we are unable to distinguish any further complexity in the spectral characteristics.

A.4 Results and Discussion

In general, with lower temperature and increased magnetic field strength, longitudinal relaxation of ^{1}H in MEH-PPV and DOO-PPV becomes both longer and more highly nonmonoexponential, ranging from over 1000 s for DOO-PPV at 4 K and 4.7 T to a few hundred milliseconds for both materials at 150 K and above. Low SNR precluded data acquisition for $T \geq 77$ K at 1.25 T, but the trends in our data indicate that relaxation times in this regime would be on the order of 100 ms and relatively mono-exponential. In comparing the two materials, DOO-PPV has significantly longer relaxation times at the highest field measured, but this property disappears or is even reversed somewhat at lower applied fields.

Whether we approach the diffusion-limited or the fast-diffusion regimes described in Section A.2 depends on our limited knowledge of quantities such as the spin-diffusion coefficient *D*, the dipolar coupling coefficient $\overline{C}$ (via the correlation time τ_C), and the concentration *N* of paramagnetic centers. From Eq. (A.2), we find $\overline{C} \approx 7 \times 10{-}32$ cm^6/s for $\tau_C = 1$ ns. (The rationale for choosing $\tau_C \approx 1$ ns comes from the observed T_1 minimum, discussed at length below.) Even if the diffusion coefficient is assumed to have a large range from 10^{-12} cm^2/s to as low as 10^{-16} cm^2/s, the range for the

psuedopotential radius in Eq. (A.4) is about 1-10 nm. For longer τ or larger B_0, this range decreases as $\tau_C^{-1/2}$. From Eq. (A.3), we calculate a range for the barrier radius b of about 1-10 lattice constants, where the higher end of that range corresponds to B_0 = 4.7 T and T = 4 K. If we take a to correspond to typical bond lengths of 1-1.5 angstroms, we see that we cannot reasonably assume a significant separation in length scales for ρ and b. Additionally, if we assume the diffusion-limited regime, we can calculate N from Eq. (A.6) for reasonable values of $D = 10^{-14}$ cm^2/s, τ_C = 1 ns, and T_1 = 1 s, obtaining $N = 4\times10^{12}$ cm^{-3}. On the other hand, assuming the slow-diffusion regime with $b = 10^{-7}$ cm, τ_C = 1 ns, and T_1 = 1 s yields $N = 3\times10^{18}$ cm^{-3}. These are almost certainly extreme values for N, with the actual number likely lying somewhere between the more reasonable values of 10^{14} cm^{-3} and 10^{16} cm^{-3}. These calculations lead us to conclude that our experimental parameters lie between the fast diffusion and diffusion-limited regimes.

Although Eq. (A.1) cannot be solved analytically in this intermediate regime, our essential hypothesis of proton relaxation (with associated spin diffusion) to paramagnetic centers is supported by two key features of the data shown in Figure A.3. First, we observe predominantly nonmonoexponential relaxation across most values of field and temperature—a signature of the nonuniform spin temperature resulting from spin diffusion towards discrete localized centers of relaxation in the bulk material. In fact, there is considerable evidence in the literature to suggest that paramagnetic centers of several varieties could be present in OSECs. Materials such as DOO-PPV and MEH-PPV are of interest for organic spintronics precisely because lattice impurities create

trapped electronic states between the HOMO and LUMO bands. [29] If carriers are injected electrically or via photoexcitation into the material, these states are observable as precursor pairs in spin-dependent dissociation and recombination processes. [30] Since, in this work, we studied these materials with no applied bias or illumination, such carriers may still exist in our samples but in much lower concentration. Other fixed paramagnetic centers can result from defects, vacancies, or dangling bonds that are not necessarily associated with conduction in the pi-conjugated chain, all of which are known to exist in significant densities in pi-conjugated semiconducting polymers. [31] Whether charge carriers in such localized precursor-pair states are some significant fraction of the paramagnetic centers responsible for ^{1}H T_1 relaxation in these materials remains an open question that might be addressed through similar T_1 measurements performed with samples under illumination to generate such pairs. From the standpoint of nuclear relaxation, localized or only slightly delocalized charge carriers would produce the same basic relaxation characteristics in the solid as ordinary paramagnetic centers in insulating materials. [14]

It is important to note that free rotations of the terminal CH_3 groups on the polymer side chains have thermal activation energies in the 0.06 - 0.1 eV range, and therefore may not be completely frozen out close to room temperature. This motion and an associated correlation time on order 1-10 ns, and therefore can produce fluctuations in the local magnetic fields with frequency on order ω_I with the potential to relax nearby nuclear spins. Since this motion would be possible in all terminal CH_3 groups in all polymer

chains, any relaxation of nuclear spins associated with this mechanism would be uniform across the sample, and would therefore suppress nonmonoexponential relaxation behavior, as is observed in our 4.7 T data sets

A second key feature of the data is an apparent minimum value in T_1 (considering either the $T_{1/2}$ values in Table A.1 or the dominant peaks in the T_1-spectra of Figure A.3 somewhere between 77 K and room temperature for both of the higher applied fields of 2.5 T and 4.7 T. Regardless of how close the system is to either limiting regime of spin diffusion in Eq. (A.1), the theory predicts such a minimum to occur for $\omega_I^2 \tau_C^2 \approx 1$, from which we can extract an associated correlation time of $\tau_C \approx$ 1-2 ns. While electron spin-relaxation times in solids vary widely according to material, temperature and applied field, [32] this is a reasonable time scale for relaxation of paramagnetic centers in paramagnetic salts, [33,34] bulk inorganic semiconductors, [35] and glasses doped with iron oxides, [36] particularly at 77 K and above [37]. However, it is a much shorter than that reported by Baker *et al.* (≥ 36 μs) in their study of spin dephasing of polaron pairs in MEH-PPV at room temperature, where coherence times (ultimately limited by the polaron T_1) can be quite long. More generally, the weaker spin-orbit coupling in organic materials would argue for longer values of τ_C than those observed in typical high-Z inorganic materials, as the prevalent relaxation mechanisms generally have to do with direct or indirect (Raman) phonon processes that modulate the spin-orbit interaction. In any case, we would generally expect τ_C to decrease with temperature, and thus for the

longest T_1 values to be measured at the highest applied fields and lowest temperatures ($\omega_I^2 \tau_C^2 >> 1$).

The distribution of chain lengths and the strongly disordered packing of the chains in these materials plays a critical role in any relaxation mechanism that depends on spin diffusion. The strong dipolar coupling of nearby ^{1}H nuclei in both of these materials leads to large dipolar linewidth, corresponding to $T_2 \leq$ 20 μs, whereby we note that the receiver deadtime (5 − 10 μs) precludes a more precise characterization of the transverse relaxation and NMR spectrum. This strong coupling would lead to a large spin-diffusion coefficient: using Bloembergen's original estimate of $D \sim a^2 / 50T_2$, we calculate $D \approx 1\times10^{-13}$ cm^2/s using reasonable values of a = 0.1 nm and T_2 = 20 μs. However, this would apply only to protons along a single polymer chain and perhaps to places where protons on separate chains happen to lie close enough together for dipolar coupling to be important. The DOO-PPV sample was synthesized with a nominal target value of 20 monomers per chain, whereas the nominal value for the MEH-PPV sample is > 380. In both cases, the concentration of paramagnetic centers is almost certainly much less than one per chain, and effective relaxation by spin diffusion must therefore include hopping from chain to chain. Such hopping is likely to be characterized by a much smaller diffusion coefficient than calculated above. Multimode diffusion with at least two very different diffusion coefficients, even within either analytically describable limiting regime, likely leads to a complicated T_1 spectrum that is difficult to interpret, in terms of matching the behavior of particular relaxation components to the theory presented in

Section A.2.

A.5 Conclusion

We have presented a systematic study of proton spin-lattice relaxation times in two widely studied OSECs as a function of both temperature and applied magnetic field. These measurements have identified nuclear spin diffusion to paramagnetic impurities as a dominant relaxation mechanism in these solids, which produces the multi-exponential relaxation behavior observed in many of our measurements. To analyze this multiexponential relaxation behavior, we have implemented a Laplace transform algorithm to transform relaxation measurements into T_1 spectra, which have been plotted as a function of temperature and magnetic field strength. Thus, although our experimental parameters place our system of study somewhere between the two most common analytically-solvable regimes of Eq. (A.1), our hypothesis of diffusion to paramagnetic centers as the dominant relaxation mechanism in OSECs is supported by (1) our observation of nonmonoexponential relaxation behavior across a range of temperatures and magnetic fields, and (2) the identification of a T_1 minimum value which gives a reasonable estimate of the lifetime of the trapped electronic states likely serving as the paramagnetic centers of relaxation in these materials. In addition to identifying a likely mechanism for nuclear spin relaxation in OSECs, knowledge of nuclear T_1 values could prove helpful as attempts to hyperpolarize nuclei in OSECs through dynamic nuclear polarization (DNP) methods such as CIDNP or OPNMR

continue. Since our data show nuclear T_1s to be much longer than lifetimes of typical electronic spin states in OSECs, it is unlikely to be a limiting factor in any such experiment.

A.6 Acknowledgements

We acknowledge helpful discussions with K. van Schooten, A. Thiessen, and C. Boehme. We are also grateful to L. Wojcik for synthesizing the DOO-PPV. This work was supported by the National Science Foundation (NSF) Materials Research Science and Engineering Center (MRSEC) at the University of Utah (Grant No. DMR11-21252), as well as NSF Grant No. DMR-1104495.

Table A.1

Values of $T_{1/2}$, in seconds, for ^{1}H in the organic semiconducting polymers MEH-PPV and DOO-PPV as a function of applied magnetic field and temperature. The parameter $T_{1/2}$ is the time for recovery of magnetization from an initially unpolarized state to half of its thermal-equilibrium value. Values shown in the "~ 150 K" row were taken at temperatures near 150 K, where the temperature drift as the cryostat warmed to room temperature from 77 K was slowest. (Specific values for each measurement are given in Figure A.3.)

DOO-PPV			
	4.7 T	**2.5 T**	**1.25 T**
4 K	1130 ± 35	3.75 ± 0.10	15 ± 1
10 K	225 ± 10	0.70 ± 0.04	6.3 ± 0.2
50 K	4.1 ± 0.1	8.4 ± 0.4	- -
77 K	4.4 ± 0.1	2.4 ± 0.1	1.52 ± 0.06
~ 150 K	0.29 ± 0.01	0.165 ± 0.005	- -
291 K	0.44 ± 0.02	0.260 ± 0.005	- -
MEH-PPV			
	4.7 T	**2.5 T**	**1.25 T**
4 K	9.0 ± 0.5	37.5 ± 4.5	16.3 ± 0.4
10 K	50 ± 2	8.6 ± 0.7	0.45 ± 0.10
50 K	15.0 ± 0.5	4.0 ± 0.2	- -
77 K	1.40 ± 0.25	1.5 ± 0.1	- -
~ 150 K	0.29 ± 0.01	0.24 ± 0.01	- -
219 K	0.34 ± 0.01	0.25 ± 0.01	- -

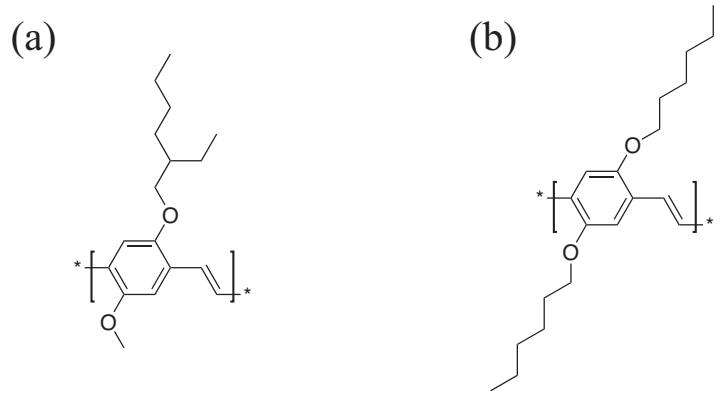

Figure A.1 MEH-PPV and DOO-PPV molecular structures. Molecular structures for (a) MEH-PPV (260.18 Da per monomer) and (b) DOO-PPV (358 Da per monomer). Bond lengths vary between 0.1 - 0.15 nm, but the disordered packing behavior of the long polymer chains can cause spacing between adjacent chains to be much larger.

Figure A.2 Laplace transform analysis of nonmonoexponential T_1 decay. (a) Magnetization recovery of ^{1}H vs. time in DOO-PPV at 1.25 T and 77 K. This is a relatively rare instance in these measurements where the decay fits reasonably well to a single exponential. The boxed graph shows corresponding Laplace transform having a single peak corresponding to $T_1 = 2.28 \pm 0.04$ s (uncertainty extracted from the fit to the time-domain data). (b) Magnetization recovery of ^{1}H vs. time in MEH-PPV at 2.5 T and 10 K. Here, the decay is strongly nonmonoexponential. The boxed graph shows corresponding Laplace transform which shows many peaks, some of which are not reflected in the multiexponential fit to the time-domain data.

(a)

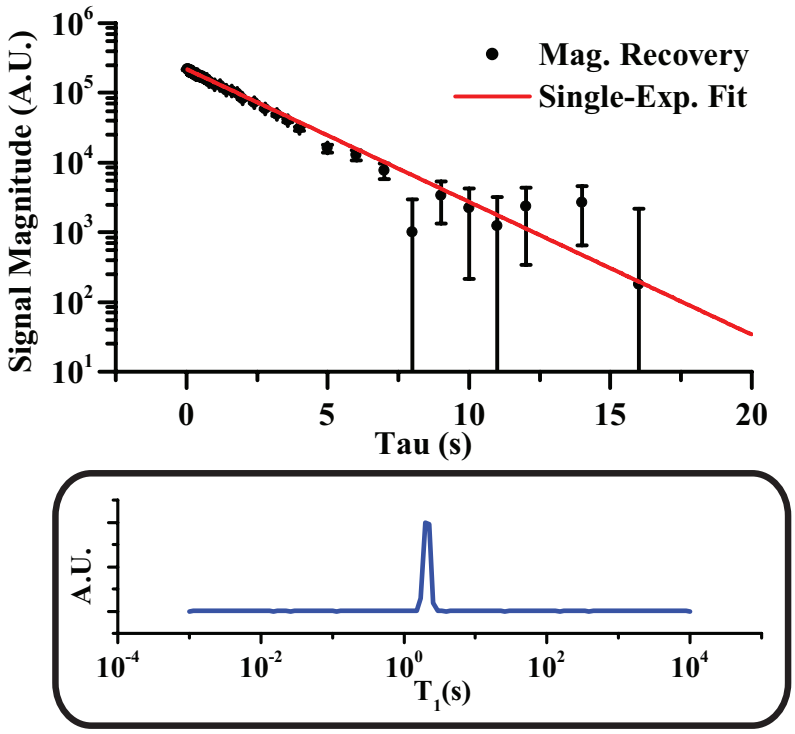
Signal Magnitude (A.U.)
Mag. Recovery
Single-Exp. Fit
Tau (s)
A.U.
T1(s)

(b)

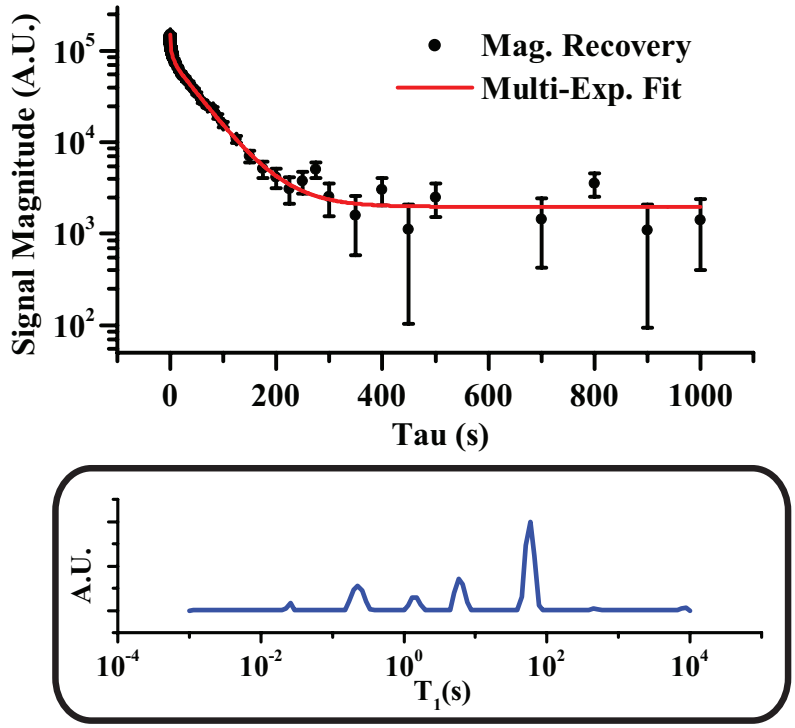
Signal Magnitude (A.U.)
Mag. Recovery
Multi-Exp. Fit
Tau (s)
A.U.
T1(s)

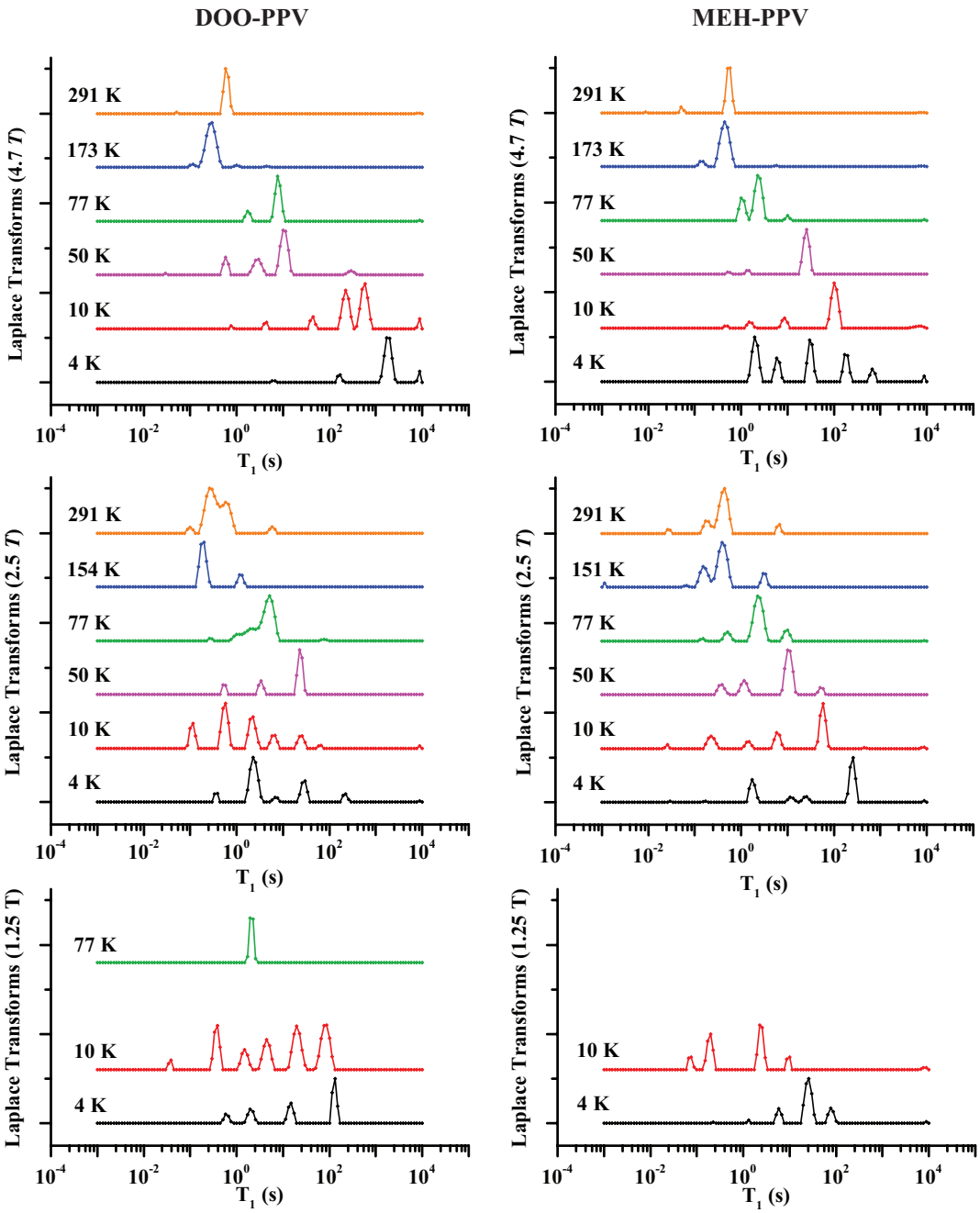

Figure A.3 Laplace transform analysis of MEH-PPV and DOO-PPV T1 data. Relaxation spectra for ^{1}H in DOO-PPV and MEH-PPV, determined by taking the Laplace transform of time-domain saturation-recovery data. If one assumes a multi-exponential decay model, then the intensities correspond to the weights of the various T_1 components. Nonmonoexponential behavior, in general, tends to be most prevalent at lowest temperatures and highest fields. Significant dependence of the relaxation behavior on both temperature and magnetic field is observed; the largest T_1 component may pass through an apparent minimum between 77 K and room temperature.

A.7 References

[1] E. F. Thenell, M. E. Limes, E. G. Sorte, Z. V. Vardeny, and B. Saam, Phys. Rev. B **91**, 045205 (2015)

[2] Organic Spintronics, edited by Z.V. Vardeny, CRC Press (2010)

[3] T.D. Nguyen *et al*., Nat. Materials **9**, 345 (2010).

[4] I. Appelbaum, B. Huang, and D.J. Monsma, Nature **447**, 295 (2007)

[5] Z.H. Xiong, D. Wu, Z.V. Vardeny, and J. Shi, Nature **427**, 821 (2004).

[6] T.D. Nguyen, E. Ehrenfreund, and Z.V. Vardeny, Science **337**, 204 (2012).

[7] W.J. Baker *et al*., Nat. Commun. **3**, 898 (2012).

[8] W.J. Baker, T.L. Keevers, J.M. Lupton, D.R. McCamey, and C. Boehme, Phys. Rev. Lett., **108**, 267601 (2012)

[9] E. Daviso, G. Jeschke, and J. Matysik in Biophysical Techniques in Photosynthesis II, ed. T.J. Aartsma and J. Matysik (Springer, Dordrecht, 2008), p. 385.

[10] S.E. Barrett, R. Tycko, L.N. Pfeiffer, and K.W. West, Phys. Rev. Letters **72**, 1368 (1994).

[11] D.R. McCamey, S.Y. Lee, S.Y. Paik, J.M. Lupton, and C. Boehme, Phys. Rev. B **82**, 125206 (2010).

[12] S.-Y. Lee, *et al.*, J. Am. Chem. Soc. **133**, 072019 (2011).

[13] E. Fukushima and E.A. Uehling, Phys. Rev. **173**, 366 (1968).

[14] N. Bloembergen, Physica (Utrecht) **20**, 1130 (1954).

[15] A. Abragam, *Principles of Nuclear Magnetism* (Oxford University Press, Oxford, UK, 1961), p. 389.

[16] R.J. Fitzgerald, M. Gatzke, D.C. Fox, G.D. Cates, and W. Happer, Phys. Rev. B **59**, 8795 15 (1999).

[17] A.J. Vega, P.A. Beckmann, S. Bai, and C. Dybowski, Phys. Rev. B **74**, 214420 (2006).

[18] N.N. Kuzma, B. Patton, K. Raman, and W. Happer, Phys. Rev. Lett. **88**, 147602 (2002).

[19] P.A. Beckmann, S. Bai, A.J. Vega, and C. Dybowski, Phys. Rev. B **74**, 214421 (2006).

[20] N. Bloembergen, Physica (Utrecht) **15**, 386 (1949).

[21] A.M. Panich, C.L. Teske, and W. Bensch, Phys. Rev. B **73**, 115209 (2006)

[22] A. Abragam, *Principles of Nuclear Magnetism* (Oxford University Press, Oxford, UK, 1961), p. 380.

[23] E. Fukushima and S.B.W. Roeder, *Experimental Pulse NMR: A Nuts and Bolts Approach*, Addison-Wesley (1981).

[24] D.D. Wheeler and M.S. Conradi, Concepts Magn. Reson. A **40A**, 1 (2012).

[25] S.W. Provencher, Comp. Phys. Comm. **27**, 229 (1982)

[26] P.G. de Gennes, J. Phys. Chem. Solids **7**, 345 (1958).

[27] W.E. Blumberg, Phys. Rev. **119**, 79 (1960).

[28] G.R. Khutsishvili, Sov. Phys. Uspekhi **11**, 802 (1969).

[29] H. Meyer, D. Haarer, H. Naarmann, and H.H. Horhold, Phys. Rev. B **52**, 2587 (1995).

[30] J. Behrends, K. Lips, and C. Boehme, Phys. Rev. B **80**, 045207 (2009).

[31] A. Moliton and R.C. Horns, Polymer International **53**, 1397 (2004).

[32] R. Lopez in Computational and Instrumental Methods in EPR, edited by C. Bender and L.J. Berliner (Springer, United States, 2007), pp. 31-82.

[33] G. Ablart and J. Pescia, Phys. Rev. B **22**, 1150 (1980).

[34] M. Nogatchewsky, G. Ablart, and J. Pescia, Solid State Commun. **24**, 493-497 (1977).

[35] T.F. Boggess, J.T. Olesberg, C. Yu, M.E. Flatte, and W.H. Lau, Appl. Phys. Lett. **77**, 1333 (2000).

[36] T. Bouhacina, G. Ablart, J. Pescia, and Y. Servant, Solid State Commun. **78**, 573-577 (1991).

[37] J.S. Colton, M.E. Heeb, P. Schroeder, A. Stokes, L.R. Wienkes, and A.S. Bracker, Phys. Rev. B **75**, 205201 (2007).